

# Measurement report: Assessing the Impacts of Emission Uncertainty on Aerosol Optical Properties and Radiative Forcing from Biomass Burning in Peninsular Southeast Asia

Yinbao Jin<sup>1</sup>, Yiming Liu<sup>\*1</sup>, Xiao Lu<sup>1</sup>, Xiaoyang Chen<sup>2</sup>, Ao Shen<sup>1</sup>, Haofan Wang<sup>1</sup>, Yinpeng Cui<sup>1</sup>, Yifei Xu<sup>1</sup>, Siting Li<sup>1</sup>, Jian Liu<sup>1</sup>, Ming Zhang<sup>4</sup>, Yingying Ma<sup>3</sup>, Qi Fan<sup>\*1,5,6</sup>

<sup>1</sup>School of Atmospheric Sciences, Sun Yat-Sen University, Zhuhai 519082, China

<sup>2</sup>Institute of Tropical and Marine Meteorology, China Meteorological Administration, Guangzhou, 510000, China

<sup>3</sup>State Key Laboratory of Information Engineering in Surveying, Mapping and Remote-sensing, Wuhan University, Wuhan 430079, China

<sup>4</sup>Hubei Key Laboratory of Critical Zone Evolution, School of Geography and Information Engineering, China University of Geosciences, Wuhan 430074, China

<sup>5</sup>Southern Marine Science and Engineering Guangdong Laboratory, Zhuhai 519082, China

<sup>6</sup>Guangdong Province Key Laboratory for Climate Change and Natural Disaster Studies, School of Atmospheric Sciences, Sun Yat-sen University, Guangzhou 510275, China

Correspondence to: Qi Fan (eesfq@mail.sysu.edu.cn) and Yiming Liu (liuym88@mail.sysu.edu.cn)

## Abstract.

Despite significant advancements in improving the dataset for biomass burning (BB) emissions over the past few decades, uncertainties persist in BB aerosol emissions, impeding the accurate assessment of simulated aerosol optical properties (AOPs) and direct radiative forcing (DRF) during wildfire events in global and regional models. This study assessed AOPs (including aerosol optical depth (AOD), aerosol absorption optical depth (AAOD), and aerosol extinction coefficients (AEC)) and DRF using eight independent BB emission inventories applied to the WRF-Chem model during the BB period (March 2019) in Peninsular Southeast Asia (PSEA), where the eight BB emission inventories were the Global Fire Emissions Database version 4.1s (GFED), Fire Inventory from NCAR version 1.5 (FINN1.5), the Fire Inventory from NCAR version 2.5 MOS (MODIS fire detections, FINN2.5 MOS), the Fire Inventory from NCAR version 2.5 MOSVIS (MODIS+VIIRS fire detections, FINN2.5 MOSVIS), Global Fire Assimilation System version 1.2s (GFAS), Fire Energetics and Emissions Research version 1.0 (FEER), Quick Fire Emissions Dataset version 2.5 release 1 (QFED), and Integrated Monitoring and Modelling System for Wildland FIRES Project version 2.0 (IS4FIRES), respectively. The results show that in the PSEA region, organic carbon (OC) emissions in the eight BB emission inventories differ by a factor of about 9 (0.295-2.533  $T_g M^{-1} Tg M^{-1}$ ), with  $1.09 \pm 0.83 T_g M^{-1} Tg M^{-1}$  and a coefficient of variation (CV) of 76%. High-concentration OC emissions occurred primarily in savanna and agricultural fires. The OC emissions from the GFED and GFAS are significantly lower than the other inventories. The OC emissions in FINN2.5 VISMOS are approximately twice as high as those in FINN1.5. Sensitivity analysis of AOD simulated by WRF-Chem to different BB emission datasets indicated that the FINN scenarios (v1.5 and 2.5) significantly overestimate AOD compared to observation (VIIRS), while the other inventories underestimate AOD in the high AOD (HAOD, AOD>1)

带格式的: 上标

35 regions range from 97-110°E, 15-22.5°N. Among the eight schemes, IS4FIRES and FINN1.5 performed better in terms of  
36 AOD simulation consistency and bias in the HAOD region when compared to AERONET sites. The AAOD in WRF-Chem  
37 during the PSEA wildfire period was assessed using satellite observations (TROPOMI) and AERONET data, and it was found  
38 that the AAOD simulated with different BB schemes did not perform as well as the AOD. The significant overestimation of  
39 AAOD by FINN (v1.5 and 2.5), FEER, and IS4FIRES schemes in the HAOD region, with the largest overestimation for  
40 FINN2.5 MOSVIS. FINN1.5 schemes performed better in representing AAOD at AERONET sites within the HAOD region.  
41 The simulated AOD and AAOD from FINN2.5 MOSVIS always show the best correlation with the observations. AEC  
42 simulated by WRF-Chem with all the eight BB schemes trends were consistent with CALIPSO in the vertical direction (0.5  
43 km to 4 km), demonstrating the efficacy of the smoke plume rise model used in WRF-Chem to simulate smoke plume heights.  
44 However, the FINN (v1.5 and 2.5) schemes overestimated AEC, while the other schemes underestimated it. In the HAOD  
45 region, BB aerosols exhibited a daytime shortwave radiative forcing of  $-32.60 \pm 24.50 \text{ W m}^{-2}$  at the surface, positive  
46 forcing ( $1.70 \pm 1.40 \text{ W m}^{-2}$ ) in the atmosphere, and negative forcing ( $-30.89 \pm 23.6 \text{ W m}^{-2}$ ) at the top of the atmosphere.  
47 Based on the analysis, FINN1.5 and IS4FIRES are recommended for accurately assessing the impact of BB on air quality and  
48 climate in the PSEA region.

带格式的: 上标

## 49 1 Introduction

50 Peninsular Southeast Asia (PSEA), including Vietnam, Thailand, Myanmar, Cambodia, and Laos, is one of the major biomass  
51 burning (BB) emission source areas in the world (Yadav et al., 2017). Due to widespread forest fires and agro-residue burning,  
52 extensive BB activities occur over PSEA, especially during the dry season (BB usually peaks in March) (Reddington et al.,  
53 2021) and release large amounts of aerosols and trace gases (including organic carbon (OC), black carbon (BC), particulate  
54 matter (PM), nitrogen oxides (NO<sub>x</sub>), and volatile organic compounds (VOC)) into the air, thus leading to significant impacts  
55 on atmospheric composition, radiative budget, and human health (Reid et al., 2013). Therefore, it is crucial to understand the  
56 BB emission inventories, as well as the behavior of aerosols, and accurately model their properties, to assess their impact on  
57 air quality and climate change in the PSEA region.

58 Numerous studies have been conducted to assess the effects of BB emissions on aerosol optical properties (AOPs), such as  
59 aerosol optical depth (AOD), absorbing aerosol optical depth (AAOD), and aerosol extinction coefficient (AEC), as well as  
60 direct radiative forcing (DRF) in the PSEA region (Zhu et al., 2017; Lin et al., 2014; Dong and Fu, 2015a). However, most of  
61 these studies have relied on only one single BB emission inventory without comparing different inventories, leading to large  
62 uncertainties in assessing the impact of BB aerosols. Due to the challenges in directly measuring BB emissions, various global  
63 fire emissions inventories have been developed based on satellite observations in the past decades (Ichoku and Ellison, 2014;  
64 Wiedinmyer et al., 2023; Wiedinmyer et al., 2011). These inventories use different empirical methods and underlying data to  
65 represent gas and aerosol emissions from fires, resulting in inherent uncertainties (Carter et al., 2020).

66 These uncertainties arising from different BB emissions often manifest as regional variations and inconsistencies with  
67 observations when integrated into models (Liu et al., 2020). Addressing these uncertainties is crucial for refining climate  
68 models and providing more accurate projections of future climate change. For example, Pan et al. (2020) compared six BB  
69 aerosol emission datasets from 2008 globally as well as from 14 regions, and the total global emissions from these BB emission  
70 datasets differed by a factor of 3.8. Sensitivity analysis of AOD simulated by Goddard Earth Observing System-Chemistry  
71 (GEOS-Chem) to different BB emission datasets during the peak BB period in each region and at most AERONET sites in  
72 each region found that Quick Fire Emissions Dataset version 2.4 (QFED2.4) produced the highest AOD values, closest to  
73 observations, followed closely by Fire Energetics and Emissions Research version 1.0 (FEER1.0). In the North American  
74 region, the GEOS-Chem incorporating four different BB emission inventories and remote-sensing data analysis during wildfire  
75 periods indicated a 4 to 7-fold difference in BB aerosol emissions. Simulations driven by Global Fire Emissions Database  
76 version 4s (GFED4s) and Global Fire Assimilation System version 1.2 (GFAS1.2) provide better agreement with surface  
77 measurements of organic aerosol and BC mass concentrations, BC observations at higher altitudes, and Moderate Resolution  
78 Imaging Spectroradiometer (MODIS) observations of AOD (Carter et al., 2020). To explore the uncertainty of BB emissions  
79 in the tropics, GFED V3, Fire INventory from NCAR version 1 (FINN1.0), and GFAS1 were used to evaluate Global Model  
80 of Aerosol Processes (GLOMAP) model simulations of AOD in South America, Africa, and Southeast Asia showing that the  
81 model underestimates AOD for all emission datasets (Reddington et al., 2016). In the North Sub-Saharan Africa BB region,  
82 Zhang et al. (2014) found a 12-fold difference in estimates of total smoke emissions and an even larger difference (up to 33-  
83 fold) in WRF-Chem simulated smoke-related variables and radiative effects. Wiedinmyer et al. (2023) have shown that the  
84 seasonal cycle (averaged over 2012-2019) of CO emissions from BB in various regions of the world and the latest version of  
85 FINN v2.5 (MODIS+ VIIRS) has an emission peak in March, primarily driven by emissions from the PSEA. However, this  
86 peak is absent in GFED and is less pronounced in other emission inventories (FINN1.5, FEER, GFAS, QFED) during the PSEA  
87 march BB peak, only the FINN2.5 captures the feature, which is not seen in GFED and as pronounced in other inventories  
88 (Wiedinmyer et al., 2023). Despite substantial research efforts, accurately representing BB aerosols in models remains a  
89 challenge. In summary, compared to the differences between global BB emission inventories, regional differences may be  
90 larger, especially in the PSEA region, where the satellite inversions of BB contain a large fraction of uncertainty due to high  
91 cloud cover (Dong and Fu, 2015b). Significant differences exist in AOPs and radiative forcing simulated by different emission  
92 inventories in the high BB emission region within a single model (Carter et al., 2020; Zhang et al., 2014). To reduce  
93 uncertainties, it is necessary to compare the differences between commonly used BB emission inventories and evaluate the  
94 model simulations of AOPs and radiative effects for the PSEA region.

95 In March 2019, the National Aeronautics and Space Administration (NASA) used remote sensing data from Visible Infrared  
96 Imaging Radiometer Suite (VIIRS) to discover hundreds of fires burning in the PSEA region (Jenner, Mar 18, 2019). The  
97 World Meteorological Organization's report highlights that the early part of 2019 corresponds to the El Niño cycle (from April  
98 to May, the temperature of waters beneath the surface of the tropical Pacific has notably declined) (Organization, 2019), during  
99 which meteorological conditions are more favourable for the occurrence and propagation of BB (Cochrane, 2009).

带格式的: 字体: (默认) +西文正文 (Times New Roman)

带格式的: 字体: (默认) +西文正文 (Times New Roman)

带格式的: 字体: (默认) +西文正文 (Times New Roman)

带格式的: 字体: (默认) +西文正文 (Times New Roman)

带格式的: 字体: (默认) +西文正文 (Times New Roman)

100 Additionally, Yin (2020) discovered that over the past 18 years (2001-2018), the PSEA region predominantly experienced the  
101 peak of BB activity in March each year. Fan et al. (2023) and Duc et al. (2021) confirmed that the PSEA suffered severe air  
102 quality impacts during the BB in March 2019. Therefore, centered on the period of March 2019, this study aims to analyze  
103 how emission uncertainties or differences from different BB inventories affect the spatial and temporal distribution of aerosols  
104 and their radiative effects in the PSEA region. Section 2 describes the model configuration, experimental design, and data  
105 sources. Section 3 presents a comparison of eight emission inventories in March 2019 and the results of simulating AOPs and  
106 DRF. Discussions are provided in Section 4, and the study concludes with a summary in Section 5.

带格式的: 字体: (默认) +西文正文 (Times New Roman)

带格式的: 字体: (默认) +西文正文 (Times New Roman)

带格式的: 字体: (默认) +西文正文 (Times New Roman)

带格式的: 字体: (默认) +西文正文 (Times New Roman)

带格式的: 字体: (默认) +西文正文 (Times New Roman)

带格式的: 字体: (默认) +西文正文 (Times New Roman)

带格式的: 字体: (默认) +西文正文 (Times New Roman)

## 107 2 Data and Methods

### 108 2.1 Model Description and Configuration

#### 109 2.1.1 WRF-Chem

110 The simulations were conducted using version 3.9.1.1 of the WRF-Chem online-coupled meteorology and chemistry model  
111 (Grell et al., 2005). Figure 1 depicts the simulation domain, outlined in blue (Figure 1(a)). It shows that the MODIS active fire  
112 instances during March 2019 were primarily consolidated in Laos, Cambodia, and Northern Thailand, as well as in Eastern  
113 and Western Myanmar (Figure 1(b)). Importantly, with a total of 69,771 fire counts, March 2019 saw the highest monthly peak  
114 of fires for that year (Figure 1(c)). A single domain (Figure 1) was employed, mainly focusing on the PSEA region (red line,  
115 including Vietnam, Thailand, Myanmar, Cambodia, and Laos.) and studying BB from February 26th to March 31st, 2019. The  
116 simulation period is from February 26 to March 31, 2019, where t  
117 The initial 3 days of the model simulation were used as a spin-up period. The model consisted of 27 vertical layers and one nested horizontal resolution of 27 x 27 km. The selected  
118 physical configurations included the Morrison double-moment microphysics scheme (Morrison et al., 2005), the Rapid  
119 Radiation Transfer Model (RRTMG) longwave and shortwave radiation schemes (Iacono et al., 2008), the Mellor-Yamada-  
120 Janjic (MYJ) planetary boundary layer scheme (Mellor and Yamada, 1982; Janjić, 1990), the Eta similarity surface Layer  
121 scheme (Monin and Obukhov, 1954), the Noah Land Surface Model land surface scheme (Niu et al., 2011) and the Grell 3D  
122 cumulus parameterization scheme (Grell and Dévényi, 2002). The Model for Ozone and Related chemical Tracers (MOZART)  
123 trace gas chemistry with the Model for Simulating Aerosol Interactions and Chemistry (MOSAIC with 4 bins) aerosol scheme  
124 with the Kinetic Preprocessor (KPP) library is used in the model (Emmons et al., 2010). In this study, MOSAIC uses a sectional  
125 approach to represent aerosol size distributions with four discrete size bins with glyoxal uptake into aqueous aerosols to form  
126 secondary organic aerosol (SOA) in the PSEA region by WRF-Chem, which is capable of simulating all major aerosol  
127 components, including nitrates ( $NO_3^-$ ), sulfates ( $SO_4^{2-}$ ), ammonium ( $NH_4^+$ ), BC, primary organic aerosols, and other inorganic  
128 aerosols through a thermodynamic approach, with high efficiency and accuracy for use in air quality and regional/global  
129 aerosol modeling (Zhang et al., 2018). The aerosol-radiation interactions (ARI) scheme of WRF-Chem includes the traditional  
130 aerosol direct and semi-direct effects (Baró et al., 2016). Mallet et al. (2020) and Palacios-Peña et al. (2018) found that model

131 [incorporation of ARI can effectively replicate smoke aerosol simulations, so the ARI scheme was selected for this paper.](#) The  
132 Community Atmosphere Model with Chemistry (CAM-chem) simulation outputs (Emmons et al., 2020; Buchholz et al., 2019)  
133 are used as chemical lateral boundary and initial conditions for WRF-Chem (<https://rda.ucar.edu/datasets/ds313.7/>, last access:  
134 11 May 2023). The product simulated by CAM-chem has a horizontal resolution of 0.9 degrees by 1.25 degrees and 56 vertical  
135 levels in the vertical direction. Meteorological initial and boundary conditions were obtained from the National Centers for  
136 Environmental Prediction Final Analysis data with a  $1^\circ \times 1^\circ$  horizontal resolution.  
137 WRF-Chem employs Mie theory to perform calculations of AOPs using MOSAIC size distributions and the complex refractive  
138 indices associated with each MOSAIC chemical constituent. Specifically, it simulates AOPs (such as AEC, single scattering  
139 albedo (SSA), and asymmetry factor for scattering) distributed in four different bands: 300, 400, 600, and 1000 nm. This study  
140 used the Ångström power law (Ångström, 1929; Martinez-Lozano et al., 1998) to derive the model at 550 nm for AOD, and  
141 the detailed calculation procedure follows Kumar et al. (2014) and Saide et al. (2013). In addition, the aerosol direct radiative  
142 feedback was coupled with the RRTMG for both shortwave (SW) and longwave (LW) radiation as implemented by Zhao et  
143 al. (2010). A detailed description of the computation of AOPs and DRF in WRF-Chem has been given by Fast et al. (2006),  
144 Zhao et al. (2011), and Lin et al. (2014).

### 145 **2.1.2 Anthropogenic and Biogenic Emissions**

146 The latest version of the global anthropogenic emissions inventory, the monthly Emissions Database for Global Atmospheric  
147 Research (EDGAR) v5.0, was published by Marvin (2022) on February 17, 2022. It provides global air pollutant emissions  
148 for the year 2015 at a resolution of  $0.1^\circ \times 0.1^\circ$ . These emissions were speciated for the MOZART chemical mechanism and can  
149 be accessed at <https://zenodo.org/record/6130621> (last accessed on 11 May 2023). Biogenic emissions were calculated online  
150 within the model using the Model of Emissions of Gases and Aerosols from Nature (MEGAN) inventory developed by  
151 Guenther et al. (2012).

### 152 **2.2 BB Emission Inventories**

153 There are two primary approaches to estimating BB emission inventories: "bottom-up" and "top-down" methods (Archer-  
154 Nicholls et al., 2015). The "bottom-up" approach involves estimating emissions per species by multiplying emission factors  
155 (EF) with estimates of the biomass burned (Yevich and Logan, 2003). The latter, the "top-down" approach, bypasses the largely  
156 uncertain fuel consumption estimation step by estimating emission fluxes directly from fire radiative power (FRP) (Ichoku  
157 and Ellison, 2014). The "top-down" approach commonly utilizes AOD retrieved from satellite remote sensing to constrain  
158 aerosol emissions from wildfires (Huneus et al., 2012). This study evaluates the performance of the WRF-Chem using eight  
159 different BB emission inventories to simulate wildfires in the PSEA region during March 2019. These emission inventories  
160 include the Global Fire Emissions Database version 4.1s (GFED), Fire INventory from NCAR version 1.5 (FINN1.5), the Fire  
161 Inventory from NCAR version 2.5 MOS (MODIS fire detections, FINN2.5 MOS), the Fire Inventory from NCAR version 2.5  
162 MOSVIS (MODIS+VIIRS fire detections, FINN2.5 MOSVIS), Global Fire Assimilation System version 1.2s (GFAS), Fire

163 Energetics and Emissions Research version 1.0 (FEER), Quick Fire Emissions Dataset version 2.5 release 1 (QFED), and  
164 Integrated Monitoring and Modelling System for Wildland FIRES Project version 2.0 (IS4FIRES). Table 1 provides a detailed  
165 comparison of their spatial and temporal resolution, the main references for the EF, the satellite data sources, Non-methane  
166 hydrocarbons (NMHCs), oxygen volatile organic compounds (OVOCs), gases ( $\text{CO}$ ,  $\text{NO}_x$ ,  $\text{SO}_2$ ,  $\text{NH}_3$ ), and aerosols in the  
167 inventory. NMHCs refer to organic compounds containing only C and H besides methane ( $\text{CH}_4$ ), such as alkanes, alkenes,  
168 alkynes, etc. OVOCs contain C, H, and O compounds, e.g., alcohols, aldehydes, ketones, etc. NMHCs and OVOCs combined  
169 constitute nearly all of the non-methane volatile organic compounds (NMVOCs) emitted by wildfires (Akagi et al., 2011).

带格式的: 下标

带格式的: 下标

带格式的: 下标

#### 170 2.2.1 GFED (v4.1s)

171 The GFED4.1s datasets provide the area burned, dry matter (DM), and EF from global fires. It has a spatial resolution of  $0.25^\circ$   
172  $\times 0.25^\circ$  and can be accessed at [https://daac.ornl.gov/get\\_data/](https://daac.ornl.gov/get_data/) (last accessed on 11 May 2023). This dataset includes fractional  
173 contributions from different fire types and offers daily or 3-hourly data to scale monthly emissions to a higher temporal  
174 resolution. GFED4.1s is an enhanced version of the GFED4 dataset, incorporating small fire inputs to enhance the accuracy  
175 and completeness of emission estimates (Randerson et al., 2017). It covers the period from June 1997 to 2022 and includes a  
176 wide range of emission species such as carbon (C), DM, carbon dioxide ( $\text{CO}_2$ ), carbon monoxide (CO), methane ( $\text{CH}_4$ ),  
177 hydrogen ( $\text{H}_2$ ), nitrous oxide ( $\text{N}_2\text{O}$ ),  $\text{NO}_x$ , NMHCs, OVOCs, OC, BC, PM less than 2.5 microns in diameter ( $\text{PM}_{2.5}$ ), total PM  
178 (TPM), and sulfur dioxide ( $\text{SO}_2$ ). The raw GFED emission data ( $0.25^\circ \times 0.25^\circ$ ) were first re-gridded to the required spatial  
179 resolution for the WRF-Chem domains using the Earth System Modeling Framework (EMSF) program in Figure 2, followed  
180 by supplementing the GFED emission species (Table S1) to meet the MOZART-MOSAIC scheme based on the study by  
181 Akagi et al. (2011) and Heil A. (2020). The construction of the final emission inventory included incorporating the mean  
182 fraction and fire size of the four vegetation types (grassland, extratropical forest, savanna, tropical forest) from FINN1.5. This  
183 incorporation enables WRF-Chem to calculate the smoke plume rise (Freitas et al., 2007; 2010).

#### 184 2.2.2 FINN (v1.5, v2.5 MOS, and v2.5 MOSVIS)

185 The emissions estimation of FINN (v1.5 and 2.5 ) are based on the framework described by Wiedinmyer et al. (2011) and  
186 Wiedinmyer et al. (2023), which utilizes two types of satellite observations: (1) MODIS fire detections and (2) active fire  
187 detections from both MODIS and VIIRS. It provides global daily estimates of BB emissions for important gases and aerosols,  
188 along with comprehensive specifications of total VOC emissions for three commonly used chemical mechanisms (MOZART-  
189 T1, SAPRC99, and GEOS-Chem) in regional and global chemical transport models (<https://www.acom.ucar.edu/Data/fire/>,  
190 last accessed on 11 May 2023). Since its release, FINN has been widely utilized by researchers to assess air quality during  
191 wildfire events (Lin et al., 2014; Vongruang et al., 2017; Pan et al., 2020). The latest version, FINN v2.5, was introduced in  
192 2022 and incorporates an updated algorithm for determining fire size by aggregating adjacent fire detections. Compared to  
193 FINN1.5, FINN2.5 incorporates significant improvements in input data and processing methods for detecting fire activity,  
194 characterizing annual land use/land cover and vegetation density, estimating burned area, and applying fuel loads across

195 different global regions (Wiedinmyer et al., 2023). In this study, FINN1.5 and FINN2.5 MOS (MODIS-only fire detections),  
196 and FINN2.5 MOSVIS (MODIS+VIIRS fire detections) were used. Detailed information on emission species and factors can  
197 be found in Tables S2 and S3.

### 198 **2.2.3 GFAS (v1.2)**

199 The GFAS provides data outputs that encompass spatially gridded FRP, DM burning, and BB emissions for numerous chemical,  
200 greenhouse gas, and aerosol species (Andela et al., 2013). These data are globally available from 2003 to the present, with a  
201 regular latitude and longitude grid resolution of  $0.1^\circ \times 0.1^\circ$  ([https://ads.atmosphere.copernicus.eu/cdsapp#!/dataset/cams-](https://ads.atmosphere.copernicus.eu/cdsapp#!/dataset/cams-global-fire-emissions-gfas)  
202 [global-fire-emissions-gfas](https://ads.atmosphere.copernicus.eu/cdsapp#!/dataset/cams-global-fire-emissions-gfas), last accessed on 11 May 2023). The latest version, GFAS 1.2, includes injection height daily data  
203 (mean altitude of maximum injection and altitude of plume top), which are obtained from the plume rise model and IS4FIRES.  
204 To ensure BB data quality, quality control procedures were applied to the MODIS data. In Figure 2, it is illustrated that GFAS  
205 1.2 data put into the WRF-Chem process, where the missing emission species (Table S4) required for the MOZART-MOSAIC  
206 scheme are added by Jose et al. (2017), Andreae and Merlet (2001), and Andreae (2019) method. Additionally, the mean  
207 fraction and fire size of the four vegetation types were obtained from FINN1.5, and the 3-hour time allocation from GFED4.1s  
208 was utilized for the GFAS scheme.

### 209 **2.2.4 FEER (v1.0-G1.2)**

210 In 2005, a new algorithm was developed by Ichoku and Kaufman (2005) to calculate BB emissions directly from FRP  
211 measurements (<https://feer.gsfc.nasa.gov/data/emissions/>, last accessed on 11 May 2023). This approach aimed to overcome  
212 the delays and uncertainties associated with other variables previously used. Subsequently, their work resulted in the release  
213 of the FEER Ce v1.0 product, a global BB inventory with a resolution of  $0.1^\circ \times 0.1^\circ$ . In this study, the FEERv1.0-G1.2 product  
214 utilizes the GFASv1.2 FRP dataset to provide daily data from 2003 to the present at a spatial resolution of  $0.1^\circ \times 0.1^\circ$ . It  
215 includes species such as CO, SO<sub>2</sub>, NH<sub>3</sub>, NO<sub>2</sub>, OC, BC, PM<sub>2.5</sub>, NMHCs, among others. Notably, the GFASv1.2 dataset has also  
216 been incorporated to ensure compatibility with the MOZART-MOSAIC scheme, as depicted in Table S5.

### 217 **2.2.5 QFED (v2.5r1)**

218 QFED emissions are estimated using the FRP method and draw on the cloud correction technique developed in the GFAS.  
219 However, QFED employs a more sophisticated approach for non-observed land areas, such as those obscured by clouds (Koster  
220 et al., 2015). Fire locations and FRPs are derived from MODIS Level 2 fire products (MOD14 and MYD14) and MODIS  
221 geolocation products (MOD03 and MYD03). QFEDv2.5r1, covering the period from 2000 to 2023, provides daily average  
222 emissions at a horizontal spatial resolution of  $0.1^\circ \times 0.1^\circ$ , encompassing information on OC, BC, SO<sub>2</sub>, CO, PM<sub>2.5</sub>, and other  
223 species. It can be accessed from <https://portal.nccs.nasa.gov/datashare/ies/aerosol/emissions/QFED/v2.5r1/> (last accessed on  
224 11 May 2023). Figure 2 shows the detailed process of QFEDv2.5r1 to ensure consistency with the MOZART-MOSAIC  
225 program. Table S5 illustrates the addition of missing data.

## 226 2.2.6 IS4FIRES (v2.0)

227 IS4FIRES is based on a reanalysis of FRP data obtained from the MODIS on the Aqua and Terra satellites. The dataset covers  
228 the period from 2000 to the present (Sofiev et al., 2009). IS4FIRESv2 emissions are global, with a spatial resolution of  $0.1^\circ \times$   
229  $0.1^\circ$ , provided every 3 hours, and represented in five stacked vertical layers ([http://silam.fmi.fi/thredds/catalog/i4f20emis-](http://silam.fmi.fi/thredds/catalog/i4f20emis-arch/catalog.html)  
230 [arch/catalog.html](http://silam.fmi.fi/thredds/catalog/i4f20emis-arch/catalog.html), last accessed on 11 May 2023) (Soares et al., 2015). It distinguishes between seven vegetation classes:  
231 boreal, temperate, tropical forests, residual crops, grasses, shrubs, and peat. The linear relationship between FRP and PM is  
232 based on the IS4FIRESv1 EF but scaled to vegetation class types using the BB EF described in Akagi et al. (2011). Additional  
233 IS4FIRES emission species according to Jose et al. (2017), Andreae and Merlet (2001) and Andreae (2019), Baró et al. (2021),  
234 and Wiedinmyer et al. (2011) meet the WRF-Chem selected MOZART-MOSAIC scheme (Table S5). It is noteworthy that its  
235 time allocation is processed using the self-contained 3 hours (Figure 2).

## 236 2.3 Observations and Reanalysis Data

### 237 2.3.1 Satellite observations

238 Remote sensing satellite observation is widely utilized to evaluate AOPs, as it offers several advantages (Palacios-Peña et al.,  
239 2018), including non-interference with observed samples, sensitivity to various properties, particularly AOPs relevant to  
240 wildfires, and the ability to provide different types of data products such as points, columns, or profiles (Reid et al., 2013). To  
241 assess the AOD of European wildfires simulated by WRF-Chem, Palacios-Peña et al. (2018) compared products from different  
242 satellite inversions of AOD and selected the best product for model evaluation. Following a similar research approach, we  
243 chose the following satellite products: MODIS, VIIRS, and Himawari-8. In addition, Cloud-Aerosol Lidar and Infrared  
244 Pathfinder Satellite Observation (CALIPSO) satellites were selected to evaluate AEC simulated by WRF-Chem with BB  
245 emissions. Detailed descriptions of various satellite parameters and algorithms can be found in a previous study (Ma et al.,  
246 2021).

247 For a comprehensive understanding of absorbing aerosols emitted by global/regional wildfires, the Tropospheric Monitoring  
248 Instrument (TROPOMI) on the Sentinel-5 Precursor (S5P) satellite, launched on October 13, 2017, was employed to assess  
249 AAOD (Torres et al., 2020; Filonchik et al., 2022). TROPOMI is a high spectral resolution spectrometer that covers the  
250 ultraviolet (UV) to shortwave infrared regions in eight spectral windows, offering enhanced capabilities for atmospheric  
251 monitoring compared to OMI satellites (Veeffkind et al., 2012). Operating in a push-broom configuration, TROPOMI provides  
252 a wide swath width of approximately 2600 km over the Earth's surface. The instrument boasts higher spatial resolution, wider  
253 observation range, increased sensitivity and accuracy, more measurement parameters, and higher temporal resolution, making  
254 it an advanced tool for atmospheric monitoring. The TROPOMI aerosol algorithm (TropOMAER), employed for atmospheric  
255 observations, uses observations at two near-UV wavelengths to calculate the UV Aerosol Index (UVAI) and retrieve total  
256 column AAOD and SSA (Torres et al., 2020). The AOD retrieved using TropOMAER inversion on land exhibits a root-mean-  
257 square error (RMSE) comparable to the OMI retrieval (maximum 0.1 or 30%). The RMSE of AOD over water may be two



258 times larger, while the RMSE of AAOD is estimated to be approximately 0.01 (Torres et al., 2020). For this study, the  
259 TropOMAER L2 product (<https://search.earthdata.nasa.gov/>, last accessed on 11 May 2023) with a spatial resolution of 7.5  
260 km x 3 km was selected. The WRF-Chem simulated AAOD at 500 nm was derived based on the method proposed by Hu et  
261 al. (2016), utilizing SSA (500 nm) from TROPOMI and Equation (1), where  $\lambda$  represents the wavelength. The uncertainty in  
262 SSA is approximately 0.03 (Dubovik and King, 2000)

$$\text{AAOD}(\lambda) = [1 - \text{SSA}(\lambda)] \times \text{AOD}(\lambda) \quad (1)$$

263

### 264 2.3.2 In-situ observations

265 To assess the effect of AOPs during wildfires, Baro et al. (2017) and Lin et al. (2014) first validated the meteorological field  
266 and pollutants simulated by WRF-Chem. Therefore, in this study, the FINN 1.5 scheme (the most common scheme used by  
267 WRF-Chem) was selected for validation of the model output for meteorological parameters and pollutants. The selected  
268 meteorological parameters include 2 m temperature (T2), 2 m relative humidity (RH2), and 10 m wind speed (WS10). These  
269 data were obtained from the data-sharing website (<https://rp5.ru/>, last accessed on 11 May 2023) and their global weather  
270 station identifications can be found in Table S6. The PM<sub>2.5</sub> data used to assess the stability of the model were collected from  
271 multiple publicly available website datasets from China (<https://quotsoft.net/air/>, last accessed on 11 May 2023), Thailand  
272 (<http://air4thai.pcd.go.th/webV2/history/>, last accessed on 11 May 2023), and global public datasets ([https://aqicn.org/data-](https://aqicn.org/data-platform/covid19/)  
273 [platform/covid19/](https://aqicn.org/data-platform/covid19/), last accessed on 11 May 2023), and their locations are shown in Table S7.

274 The AERONET (AErosol RObotic NETwork) project is a collaboration between NASA and PHOTONS (PHOTométrie pour  
275 le Traitement Opérationnel de Normalisation Satellitaire; Univ. of Lille 1, CNES, and CNRS-INSU), establishes a  
276 collaborative network involving ground-based remotely sensed aerosol networks. This project has been in existence for over  
277 25 years and provides a long-term, continuous, and easily accessible public-domain database for aerosol research, including  
278 the optical, microphysical, and radiometric properties of aerosols. AOD and AAOD measurements from AERONET are based  
279 on multiple wavelength bands, including visible and near-infrared spectra. Common band ranges include 340 nm, 380 nm, 440  
280 nm, 500 nm, 675 nm, 870 nm, etc. AOD and AAOD data are classified into three levels based on data quality: level 1.0  
281 (unscreened), level 1.5 (cloud shielding and quality control), and level 2.0 (quality assurance). For this study, data at the 2.0  
282 level were used, indicating that the data underwent cloud screening and quality assurance following the detailed procedures  
283 outlined by Smirnov et al. (2000). In the absence of cloud contamination, the uncertainty in AOD was estimated to be 0.01 to  
284 0.02, depending on wavelength. AAOD was calculated using Equation (1).

### 285 2.3.3 ERA5 Reanalysis data

286 European Centre for Medium-Range Weather Forecasts (ECMWF) Reanalysis v5 (ERA5) is a global meteorological reanalysis  
287 dataset developed and maintained by the ECMWF (Hersbach et al., 2018). The ERA5 dataset is based on global observational

288 data, satellite remote sensing data, and numerical model forecast data. It uses advanced data assimilation techniques to fuse  
289 data from these different sources to produce consistent and high-quality global meteorological reanalysis data. Hourly data are  
290 available from 1979 up to the current time, and ERA5 data have a spatial resolution of  $0.25^\circ \times 0.25^\circ$  (about 25 km) at the  
291 horizontal level. In this paper, the effect of ERA5 950 hpa wind on BB aerosols is analyzed.

## 292 2.4 Methodology

293 In order to assess AOD, AAOD, AEC, and DRF using WRF-Chem with different BB inventories, apart from the FINN schemes,  
294 other emissions inventories are re-gridded and time-allocated, as shown in Figure 2. Subsequently, species are supplemented  
295 according to the gas-phase chemistry and aerosol scheme (MOZART-MOSAIC) employed by WRF-Chem. It is worth noting  
296 that all scenarios utilized fire size and vegetation type proportion data from FINN1.5 to calculate smoke plume rise. The  
297 performance of WRF-Chem model simulations against measurements is evaluated using statistical metrics (Wu et al., 2019)  
298 including the mean bias (MB), RMSE, Correlation coefficient (R), and the index of agreement (IOA) in Table S8. This research  
299 further investigated DRF over PSEA during the study period. Zhao et al. (2013) and Lin et al. (2014) were referenced for the  
300 treatment of BB aerosol radiative forcing, as shown in the following equations.

$$\text{DRF} = (F_i^\downarrow - F_i^\uparrow) - (F_{no-fire}^\downarrow - F_{no-fire}^\uparrow) \quad (2)$$

301 where  $F^\uparrow$  and  $F^\downarrow$  indicate the aerosol upward radiation flux and the aerosol downward radiation flux, respectively.  $i$  indicates  
302 that WRF-chem is added to the different BB emission inventories, and *no-fire* denoted scene without BB inventory applied.

## 303 3 Result

### 304 3.1 Inter-comparison of Eight BB Inventories.

305 Several studies have utilized OC as a measurable metric to compare variations among multiple BB inventories (Reddington et  
306 al., 2016; Carter et al., 2020). This is because OC is a major component in smoke particles from fresh BB, with mass fractions  
307 ranging from 37% to 67% depending on the fuel type (Pan et al., 2020). Figure 3 presents the spatial distribution characteristics  
308 of OC for the eight BB datasets in the study region, along with the total OC emissions in the PSEA region during March 2019.  
309 The highest OC emissions across all datasets are observed in the northern regions of Laos, Cambodia, and Thailand, as well  
310 as in eastern and western Myanmar and southern Bangladesh. Lower emissions are observed in the central regions of Myanmar  
311 and Thailand, northern Vietnam, and southern regions of China. Similar spatial distribution characteristics of OC emissions in  
312 the PSEA region during March have also been reported by Pan et al. (2020) and Reddington et al. (2021). These emissions  
313 mainly originate from shrubland, evergreen broadleaf, mixed shrubland/grassland, and dryland cropland, as classified by the  
314 WRF-Chem land use data in the PSEA (Figure S1). The eight BB emissions, ranked based on their total OC emissions (PSEA)  
315 in descending order, are FINN2.5 MOSVIS (2.533  $\text{Tg M}^{-1}\text{Tg/M}$ ), FINN2.5 MOS (2.002  $\text{Tg M}^{-1}\text{Tg/M}$ ), QFED (1.303  $\text{Tg M}^{-1}\text{Tg/M}$ ),  
316 FINN1.5 (1.214  $\text{Tg M}^{-1}\text{Tg/M}$ ), IS4FIRES (0.604  $\text{Tg M}^{-1}\text{Tg/M}$ ), FEER (0.462  $\text{Tg M}^{-1}\text{Tg/M}$ ), GFAS (0.296  $\text{Tg M}^{-1}\text{Tg/M}$ ).

317  $\text{Tg M}^{-1}\text{Tg M}^{-1}$ ), and GFED (0.295  $\text{Tg M}^{-1}\text{Tg M}^{-1}$ ). The highest OC emission in the dataset is exhibited by FINN2.5 MOSVIS, which  
 318 can be attributed to the use of updated burned area data and the inclusion of fire information from VIIRS, capturing a larger  
 319 number of small-scale fires (Wiedinmyer et al., 2023). The lowest OC emissions are provided by GFED, which may have  
 320 underestimated DM and agricultural fire EF (OC, EF=2.3  $\text{g kg}^{-1}\text{g/kg}$ ), and GFAS, which only underestimated DM. The overall  
 321 mean and standard deviation of OC for different BB emission inventories in the PSEA region was  $1.09 \pm 0.83 \text{ Tg M}^{-1}\text{Tg M}^{-1}$ ,  
 322 with a coefficient of variation (CV) of 76% (CV is defined as the ratio of the standard deviation to the mean of all inventories).  
 323 Figure 4 illustrates the total emissions of the eight emission inventories in the PSEA region during March 2019 added to the  
 324 WRF-Chem after processing (Figure 2). It also presents the percentage composition of CO, OVOCs, NMHCs, NO<sub>x</sub>, Gas (SO<sub>2</sub>  
 325 and NH<sub>3</sub>), PM<sub>2.5</sub>, PM<sub>10</sub>, BC, and OC. The total BB emissions (aerosol and gas) are ranked as FINN2.5 MOSVIS (105.7  $\text{Tg M}^{-1}\text{Tg M}^{-1}$ ),  
 326 FINN2.5 MOS (83.7  $\text{Tg M}^{-1}\text{Tg M}^{-1}$ ), FINN1.5 (41.9  $\text{Tg M}^{-1}\text{Tg M}^{-1}$ ), IS4FIRES (19.4  $\text{Tg M}^{-1}\text{Tg M}^{-1}$ ), FEER (15.4  $\text{Tg M}^{-1}\text{Tg M}^{-1}$ ),  
 327 QFED (11.1  $\text{Tg M}^{-1}\text{Tg M}^{-1}$ ), GFED (10.3  $\text{Tg M}^{-1}\text{Tg M}^{-1}$ ), and GFAS (9.9  $\text{Tg M}^{-1}\text{Tg M}^{-1}$ ). Although the total QFED  
 328 emissions are low, the aerosol emissions (OC, BC, PM<sub>2.5</sub>, PM<sub>10</sub>) are not, just smaller than the FINN schemes. The PSEA  
 329 aerosol emissions from FINN2.5 are higher than those predicted for FINN1.5 and approximately twice as high as the latter,  
 330 consistent with the findings of Wiedinmyer et al. (2023). Among them, the highest and lowest emissions of OC+BC are  
 331 observed in FINN2.5 MOSVIS (2.82  $\text{Tg M}^{-1}\text{Tg M}^{-1}$ ) and GFAS (0.32  $\text{Tg M}^{-1}\text{Tg M}^{-1}$ ), respectively. Since the FINN schemes  
 332 employ the EF from Akagi et al. (2011) and subsequent updates, the proportions of each species are relatively similar. In  
 333 summary, FINN schemes (v1.5 and 2.5) have relatively high total aerosol emissions compared to the other schemes, and the  
 334 "top-down" scenario (GFAS, FEER, QFED, IS4FIRES) does not have high total emissions despite being constrained by the  
 335 AOD. To evaluate the spatiotemporal distribution characteristics of absorbing aerosols from BB emissions, particularly the  
 336 BC to OC ratio, was also displayed in Figure 4. Except for QFED, which exhibits a lower ratio of approximately 0.08 (1/13),  
 337 the ratios for the other BB datasets are greater than or equal to 0.1(1/10). Ferrada et al. (2022) found that QFED emission  
 338 inventories compared to other inventories (GFED4.1s, FINN1.5, GFAS1.2) increased BC and OC emissions by up to 5 times  
 339 in different ecological regions. In addition, differences in emission EF in Southeast Asia may result in a BC/OC equal to  
 340 approximately 0.08.

### 342 3.2 Model Validation

343 To assess the AOPs and DRF simulated by the WRF-Chem adding different BB emissions, the stability of the model is verified  
 344 by comparing the simulated meteorological fields and PM<sub>2.5</sub> concentrations with observations at monitoring stations using the  
 345 WRF-Chem with the FINN1.5 scheme. The statistical results in Table S6 demonstrate good agreement (IOA  $\geq 0.6$ ) between  
 346 the simulated T2, RH2, and WS10 and the data from 13 stations. However, at some stations, the wind speed RMSE exceeds 2  
 347  $\text{m s}^{-1}\text{s}$ , which may be attributed to unresolved topographic features in the surface drag parameterization (Saide et al., 2016).  
 348 The bias between observations and simulations for RH2 can be partially explained by the influence of different surface and  
 349 boundary layer parameterizations on the simulated near-surface water vapor fluxes (Chen et al., 2019). During the wildfire

带格式的: 上标

带格式的

带格式的: 字体:(默认) Times New Roman

带格式的

带格式的: 字体:(默认) Times New Roman

带格式的

带格式的: 字体:(默认) Times New Roman

带格式的

带格式的: 字体:(默认) Times New Roman

带格式的

带格式的: 字体:(默认) Times New Roman

带格式的

带格式的: 字体:(默认) Times New Roman

带格式的

带格式的: 字体:(默认) Times New Roman

带格式的

带格式的: 字体:(默认) Times New Roman

带格式的

带格式的

带格式的

带格式的

带格式的: 字体:(中文)+中文正文(宋体)

带格式的: 字体:(默认) Times New Roman, (中文)+中文正文(宋体)

带格式的: 字体:(中文)+中文正文(宋体)

带格式的: 字体:(默认) Times New Roman, (中文)+中文正文(宋体)

带格式的: 字体:(中文)+中文正文(宋体)

带格式的

带格式的

带格式的

带格式的

带格式的: 正文

带格式的: 上标

350 period of March 2019, the daily average observed PM<sub>2.5</sub> concentrations of 23 cities at the surface were compared with the  
351 model results for the FINN1.5 case in Figure S2, where the statistical indicators are shown in Table S7. The WRF-Chem was  
352 able to simulate PM<sub>2.5</sub> concentrations in urban sites located in the high BB emission region of northern Laos (Chiang Rai  
353 Mueang in northern Thailand and Jinghong in China) with consistency to the observed data (R of 0.64 and 0.75, respectively),  
354 where the model was able to reproduce the pollution peaks (IOA of 0.74 and 0.82, respectively). In a previous study by  
355 Vongruang et al. (2017), the WRF-CMAQ model was used to simulate PM<sub>2.5</sub> in the PSEA region by incorporating BB  
356 emissions (GFAS v1.1 or FINN1.5) and comparing them with observed stations. The average IOA value was 0.51 (with the  
357 optimal IOA being 0.69). In this study, all 23 stations had IOA values greater than 0.51 (with over 52% exceeding 0.69),  
358 indicating that the model can consistently reproduce the spatial and temporal distribution characteristics of pollutants in the  
359 PSEA region. Although the WRF-Chem model could reasonably capture the spatial-temporal characteristics of PM<sub>2.5</sub>  
360 concentrations observed in most cities (IOA > 0.54), the influence of anthropogenic emission inventories and BB vertical  
361 transport may lead to biases in some areas (e.g., Hong Kong).

### 362 3.3 AOD

#### 363 3.3.1 Satellites vs. AERONET AOD

364 The linear regression results between AOD daily averages from different satellite sensors and AERONET data are shown in  
365 Figure S3. Overall, during the wildfire event in the PSEA region, the DB algorithm of VIIRS demonstrated the best skill, as  
366 indicated by optimal R<sup>2</sup> and RMSE values. Su et al. (2022) found that VIIRS DB also exhibited the highest accuracy and  
367 stability when analyzing long-term multiple satellite inversions of AOD aerosol datasets in Asia. This is because the VIIRS  
368 DB incorporates upgraded surface and aerosol models specifically designed for Asian regions, which have not been applied to  
369 the MODIS DB (Sayer et al., 2019). Therefore, to evaluate the representation of AOD in the WRF-Chem experiments for the  
370 PSEA wildfires in March 2019, the AOD at 550 nm provided by VIIRS DB (along with AERONET observations) was chosen  
371 to determine biases and errors in the conducted experiments.

#### 372 3.3.2 WRF-Chem vs. VIIRS AOD

373 To assess the agreement between the simulated AOD from WRF-Chem and the observed AOD, we utilized the extracted data  
374 (WRF-Chem) based on VIIRS satellite transit time and compared the daily average values with AERONET observations.  
375 Figure 5 illustrates the daily average AOD at 550 nm from the VIIRS and wind (scaled in 10 m  $\cdot s^{-1}$ ) at 900 hPa (a), along with  
376 the corresponding AOD from the WRF-Chem simulation over the PSEA region during March 2019, considering different BB  
377 scenarios (b-i). The high AOD (HAOD, AOD > 1.0) derived from VIIRS retrievals is primarily concentrated in Laos, Thailand,  
378 and Vietnam (97-110°E, 15-22.5°N). Additionally, Beibu Gulf and coastal cities in southern China also exhibit high AOD  
379 values (AOD > 0.6), which may be attributed to the long-range BB transport of tropical westerly and southwesterly winds  
380 depicted in Figure 5(a). The FINN (v1.5 and 2.5), FEER, QFED, and IS4FIRES schemes demonstrate the ability to reproduce

带格式的: 上标

381 high aerosol concentrations in areas with elevated AOD values as observed by VIIRS satellites. These simulations align with  
382 the spatial distribution of monthly mean AOD during the wildfire period in the PSEA simulations conducted by Dong and Fu  
383 (2015b). However, the GFED and GFAS schemes fail to capture the high AOD areas in the PSEA region, likely due to the  
384 low BB emission inventories of the input model (Pan et al., 2020).

385 Figure 6 ((a)-1 to (a)-8) displays the estimated MB between the model with eight BB scenarios and VIIRS daily mean AOD.  
386 The FINN schemes (v1.5 and 2.5) noticeably overestimate AOD in the HAOD region, while the GFED, GFAS, FEER, and  
387 IS4FIRES schemes underestimate AOD. Moreover, the FINN schemes also exhibit AOD overestimation in the Beibu Gulf,  
388 South China Sea, Bay of Bengal, and Andaman Sea. As the FINN schemes have the largest aerosol emissions compared to  
389 other BB emissions (Figure 4), it may lead to an overestimation of AOD in the HAOD region. All schemes exhibit varying  
390 degrees of overestimation for a significant portion of southern China. Table 2 provides statistics on the MB of AOD between  
391 satellite-retrieved and WRF-Chem AOD in the HAOD region. The AOD simulated by FINN schemes are significantly  
392 overestimated, whereas the rest of the schemes exhibit underestimation. Although FEER (-0.12) and IS4FIRE (-0.14)  
393 underestimate the simulated AOD, their performance is considerably better than other BB emission inventories. As highlighted  
394 by Palacios-Pena et al. (2017) and Crippa et al. (2019), the MB between simulated and observed AOD can be attributed to  
395 estimation errors in BB uncertainty, aerosol dry mass, and specifically related to the certain mass of small particles or too  
396 much moisture associated with the aerosol. The RMSE estimation (Figure 6(b)-1 to (b)-8) reveals noticeable uncertainty in the  
397 FINN schemes compared to other schemes in the HAOD and southern China, while the performance of the remaining schemes  
398 in simulating AOD in Laos and northern Thailand is unsatisfactory. The RMSE statistics in Table 2 show that the AOD  
399 simulated by the FINN2.5 schemes (MOS and MOSVIS) have greater uncertainty in the HAOD region compared to FINN1.5,  
400 and the RMSE of the other schemes are generally comparable. Figure 6(c)-1 to (c)-8 depicts the temporal R between simulated  
401 AOD and observations, with high values of R (>0.6) concentrated in Laos and northern Thailand, Myanmar, the Bay of Bengal,  
402 the Andaman Sea, and the South China Sea. The FINN2.5 MOSVIS scheme exhibits the highest R compared to other schemes  
403 in the HAOD region (Table 2), potentially due to the updated acquisition time (local time) and increased VIIRS data, leading  
404 to improved R with the observed data.

### 405 3.3.3 WRF-Chem vs. AERONET AOD

406 Figure 7 illustrates the time series of AOD at 550 nm, measured at the 16 AERONET sites marked in Figure 1, in comparison  
407 to simulated AOD from WRF-Chem with different BB emissions. These 16 sites are categorized into three major classes,  
408 namely, the satellite inversion of HAOD regions (97-110°E, 15-22.5°N, Figure 7 a-g), the adjacent HAOD area (AHAOD,  
409 Figure 7 h-l), and the downwind area (DA, Figure 7 m-p), allowing for further analysis of AOD variations during wildfire  
410 events. In the HAOD stations (Laos, Chiang Mai, Fang, Nong Khai, Son La, and Ubon Ratchathani), high aerosol loading was  
411 captured by all schemes and AERONET sites on March 15, 23, and 30, respectively. Among the sites, the Laos station  
412 performed the best in terms of simulated and observed AOD mean R and IOA for all BB scenarios, with R and IOA values of  
413 0.82 and 0.80, respectively (Table 3). To compare the performance of the multi-BB emission scenario model for the AOD

414 simulation, a Taylor diagram was constructed (Figure 8). The Taylor diagram demonstrates that, in the HAOD regions, the  
415 FINN schemes (v1.5 and 2.5) exhibit a higher overall R compared to other schemes when simulating AOD against observations.  
416 Furthermore, the FINN2.5 schemes show a slightly better correlation than FINN1.5. Among the eight schemes, the IS4FIRES  
417 and FINN1.5 schemes simulated AOD performed better in terms of consistency and deviation from the observed comparison  
418 in the HAOD region (Figure 8(a)). In the AHAOD stations, peaks of AOD simulated by WRF-Chem were also found on three  
419 dates (March 15, 23, and 30), but these peaks were lower than the HAOD in Figure 7. Despite the FINN2.5 MOSVIS scheme  
420 showing the best correlation between simulated AOD and observations in the HAOD regions compared to other schemes, its  
421 performance in AHAOD regions was unsatisfactory (Table 3). Poorly performing stations in the AHAOD regions included  
422 Bangkok, Silpakorn, and Songkhla, which are located between 0° and 22.5° N latitude (Figure 7). This discrepancy may be  
423 attributed to the assumptions made by the FINN2.5 MOSVIS scheme for fire detection in the equatorial region to achieve daily  
424 global coverage (Wiedinmyer et al., 2023) and the overestimation of AOD values by WRF-Chem, which can be explained by  
425 the presence of excess aerosol dry mass (Chapman et al., 2009). In the DA regions, such as Hong Kong and Taiwan, high  
426 concentrations of aerosols were simulated and observed after March 23 in Figure 7. Previously, studied the same event using  
427 models and ground measurements and reported a contribution of BB of about 56% to local AOD and 26%-62% to DA.

### 428 3.4 AAOD

#### 429 3.4.1 WRF-Chem vs. TROPOMI AAOD

430 Wildfire releases significant amounts of absorbing aerosols such as OC and BC, which can absorb solar radiation and increase  
431 the radiation absorption capacity of the atmosphere, thereby affecting the Earth's radiation balance. Therefore, it is crucial to  
432 evaluate the model's ability to simulate absorbing aerosols using AAOD results obtained from satellite observations. To reduce  
433 the discrepancies caused by missing data in the inversion of different observations, the WRF-Chem simulations are matched  
434 with the observed data. Figure 9 shows the spatial distribution of daily mean AAOD at 500 nm retrieved by TROPOMI (a)  
435 and simulated by WRF-Chem with eight BB emissions (b-j) during March 2019 in the PSEA region. The high AAOD (AAOD >  
436 0.03) from TROPOMI is mainly concentrated in northern Laos, northern Vietnam, and northern Thailand, and eastern Vietnam,  
437 which is similar to the spatial distribution characteristics of HAOD provided by VIIRS. Kang et al. (2017) also found similar  
438 AAOD distribution patterns when studying the spatial and temporal characteristics of absorbing aerosols in Southeast Asia  
439 from 2005 to 2016. The WRF-Chem simulations with different BB emissions exhibit high AAOD values not only in the  
440 aforementioned regions but also in southern China and the South China Sea (Figure 9). Figure 10 shows the spatial distribution  
441 characteristics of MB(a), RMSE(b), and R(c) for the comparison of TROPOMI-inverted AAOD with WRF-Chem-simulated  
442 AAOD using different BB scenarios. All FINN, FEER, and IS4FIRES schemes overestimate AAOD in the HAOD region (97-  
443 110°E, 15-22.5°N) compared to TROPOMI inversion, with FINN2.5 showing the most significant overestimation (Figure  
444 10(a)-1 to (a)-8). Table 2 further confirms these overestimations with statistics of 0.056, 0.073, 0.08, 0.02, and 0.018,  
445 respectively. The overestimation may arise from underestimating AAOD in TROPOMI, as well as overestimating absorbing

446 aerosols in the BB inventory and uncertainties in the representation of absorbing aerosols by WRF-Chem, including aerosol  
447 size distribution, chemical composition, aging processes, vertical and horizontal transport (including injection heights for fire  
448 emissions), and errors in dry/wet removal from the atmosphere. Figure 10(b)-1 to (b)-8 and Table 2 demonstrate that the FINN  
449 schemes exhibit greater uncertainties in simulating AAOD in the HAOD region compared to other schemes. Comparing the R  
450 between satellite-retrieved AAOD and simulated AAOD, values of  $R > 0.6$  are primarily concentrated in northern Laos,  
451 northern Thailand, and Myanmar. Particularly, the FINN2.5 MOSVIS scheme, due to the incorporation of improved local time  
452 and inclusion of small fires from VIIRS, exhibits the best correlation with the simulated AAOD relative to satellite retrievals  
453 (Table 2).

#### 454 **3.4.2 WRF-Chem vs. AERONET AAOD**

455 To reduce the uncertainty caused by missing AERONET data, quality control has been applied to the AERONET site data  
456 (samples  $> 10$  days). In the HAOD region within the range of  $97-110^{\circ}\text{E}$ ,  $15-22.5^{\circ}\text{N}$ , where both the satellite-retrieved AOD  
457 and AAOD exceed the thresholds of 1 and 0.03 (BB high emission area), respectively. Figure 11 presents a comparison of  
458 time series between AAOD measurements from four AERONET sites within the HAOD region and AAOD simulated by the  
459 nearest corresponding AERONET site using WRF-Chem with different BB inventories. Similar to peaks of AOD, AAOD  
460 from the Doi Ang Khang site also exhibits peaks on March 15th, 23rd, and 30th. Although most schemes can capture the high  
461 AAOD loading, the performances of the GFED, GFAS, and QFED schemes are unsatisfactory (Table S9). This could be  
462 attributed to lower concentrations of absorbing aerosols or inaccurate spatial distribution in the BB emission inventories  
463 (Reddington et al., 2016). The Fang site shows the best mean R and IOA among the eight BB scenarios simulating AAOD  
464 compared with AERONET, with R and IOA values of 0.69 (Table S9). The Taylor diagram indicates that the FINN schemes  
465 perform better than others in representing AAOD in Figure 8 (b), which may be the FINN schemes for unique calculating  
466 biomass burned area and EF that are more suitable for the HAOD region (Wiedinmyer et al., 2011; 2023). When comparing  
467 simulated AAOD with observations for the FINN2.5 MOSVIS scheme, both the R and IOA perform better than other schemes  
468 at all sites. The improved performance of the FINN2.5 MOSVIS scheme in simulating AAOD during wildfires in the PSEA  
469 region can be attributed to two factors: the inclusion of smaller fires using VIIRS 375m fire detection data and updated  
470 information on time and burned area.

#### 471 **3.5 AEC**

472 Although AOD and AAOD provide useful information about atmospheric aerosol loading, there is limited information  
473 available regarding the vertical distribution of aerosols. Palacios-Peña et al. (2018) found that uncertainty in the vertical  
474 distribution of aerosols during wildfires in Europe affects AOPs. The CALIPSO, with its unique capability to actively retrieve  
475 vertical aerosol spatial distribution, offers an opportunity to assess the simulation of aerosol vertical optical properties by  
476 WRF-Chem during wildfire events. Figure 12 displays the aerosol vertical extinction profiles at 532 nm retrieved by CALIPSO  
477 in the HAOD region during March 2019, along with the aerosol extinction profiles (550 nm) simulated by various BB schemes,

478 where model data are matched with CALIPSO overpass times. AEC retrieval by CALIPSO is greater than 0.2 within the range  
479 of 0.5 km to 4 km above ground level, possibly due to the uplifted aerosols from wildfires. WRF-Chem utilizes the smoke  
480 plume rise model, with upper and lower limits of heat flux determined for each land type, to calculate the minimum and  
481 maximum plume heights, and the emitted pollutants are distributed across each vertical layer within the injection height (Grell  
482 et al., 2011). From 0.5 km to 4 km, the trends of AEC changes in the eight BB schemes are consistent with CALIPSO,  
483 indicating that the employed smoke plume rise model in WRF-Chem can reproduce the minimum and maximum plume heights.  
484 However, all the FINN schemes overestimate AEC compared to CALIPSO from 0.5 km to 4 km, while the other schemes  
485 underestimate it. The aerosol concentration in the BB emission inventories may play a decisive role, leading to differences in  
486 the AEC (Reddington et al., 2019). Figure S4 illustrates the frequency distribution of six aerosol types at an altitude of 8 km  
487 over the PSEA region in March 2019. Within the higher altitudes of 5-7 km the presence of dust, polluted dust, and smoke  
488 aerosols is evident, with the dust aerosols originating from the upper-level westerlies in the Indian region. Within this altitude  
489 range, the simulated AEC gradually approaches zero with increasing altitude. However, the AEC retrieved by CALIPSO  
490 exhibits three peaks, which may be attributed to uncertainties in the calculation model for BB injection heights and the  
491 influence of external dust transport. At 4-8 km, the AEC gradually tends to zero with increasing altitude, while the AEC from  
492 the CALIPSO still has three peaks, which may be due to the uncertainty of the model for the BB injection height calculation  
493 or the effect of external dust transmission (Dong and Fu, 2015a; Jin et al., 2022).

### 494 3.6 DRF

495 Considering the significant impact of BB aerosols on radiation, this study investigates the radiative perturbation of SW  
496 radiation caused by BB aerosols under clear-sky conditions at the top of the atmosphere (TOA), surface (SFC), and in the  
497 atmosphere (ATM). The focus is on the DRF of BB aerosols during the daytime, as Ge et al. (2014) found that local  
498 convergence in the smoke source region caused by smoke during the daytime transmits more smoke particles on the above  
499 surface. Figure 13 illustrates the spatial distribution of daytime average SW radiative perturbation caused by BB aerosols  
500 during 2019 March in the PSEA region at the TOA, ATM, and SFC. It is evident that BB aerosol DRF exists not only in the  
501 PSEA region but also in other regions such as southern China, Hong Kong, and Taiwan. The spatial distribution of SW radiative  
502 perturbation by BB aerosols aligns with the simulated distribution of AOD, with the highest values observed in the HAOD  
503 region (97-110°E, 15-22.5°N). Lin et al. (2014) have confirmed that BB aerosols, mainly BC and OC, play significant roles in  
504 the radiative budget. On one hand, the solar absorption by BC in the atmosphere increases the rate of radiative heating, leading  
505 to a significant decrease in solar radiation reaching the surface. On the other hand, OC enhances the reflected solar radiation  
506 at the TOA, resulting in a cooling effect due to reduced incident solar radiation on the atmosphere and surface. The SW  
507 radiative perturbation of BB in TOA is negative with a cooling effect in the model domain for eight scenarios, except for areas  
508 with high surface albedo such as Himalayan glaciers. Figure 14 shows that during the wildfire period in the HAOD region, the  
509 eight schemes exhibit DRF of  $-30.89 \pm 23.6 \text{ W m}^{-2} \text{ W/m}^2$  at TOA. The SW radiative perturbation of BB aerosol at TOA depends  
510 largely on the SW absorption rate of BB aerosol. The FINN schemes (v1.5 and 2.5) exhibit a significantly stronger cooling



511 effect compared to other schemes, possibly due to higher BC concentrations in BB emissions compared to other inventories.  
512 At the ATM, the absorption by BB aerosols leads to a positive radiative forcing, causing atmospheric warming, particularly in  
513 the HAOD region. In the HAOD region, the eight schemes exhibit a BB aerosol SW DRF of  $1.70 \pm 1.40 \text{ W m}^{-2} \text{ W/m}^2$  in the  
514 ATM (Figure 14). WRF-Chem can simulate the heating effect of BB aerosols in the ATM regardless of the BC/OC ratio used  
515 in the emission inventory (1:8, 1:9, or 1:13). At the SFC, the cooling effect is due to the scattering of non-absorbing atmospheric  
516 aerosols and absorbing aerosols that increase the radiative heating rate, resulting in a significant reduction of solar radiation  
517 reaching the surface. The eight schemes simulate the DRF of  $-32.60 \pm 24.50 \text{ W m}^{-2} \text{ W/m}^2$  at SFC in the daytime (with FINN2.5  
518 MOSVIS reaching a maximum of approximately  $70 \text{ W m}^{-2} \text{ W/m}^2$  (Figure 10), which is comparable to the level of the PSEA  
519 region studied previously by Lin et al. (2014) and Ge et al. (2014).

#### 520 4. Discussion

521 Biases in the simulated AOPs (AOD, AAOD, AEC) over tropical BB have been attributed to a variety of factors (Reddington  
522 et al., 2016), including (1) uncertainties in BB emission fluxes, (2) errors in modeling the atmospheric distribution and  
523 properties of BB aerosols. These deviations in optical properties further affect the DRF, leading to uncertainties in the  
524 assessment of climate change.

##### 525 4.1 BB Emission Fluxes

526 Uncertainties associated with the derivation of emission fluxes arise from errors in satellite detection of active fire or burned  
527 areas (e.g., cloud and smoke obscuration of the surface, satellite spatial resolution and detection limitations, and satellite  
528 exceedance times), as well as uncertainties in EF and fuel consumption estimates (Carter et al., 2020; Wiedinmyer et al., 2023).  
529 Eight BB inventories were inverted from MODIS data, but there were significant gaps between the bandwidths of MODIS in  
530 the equatorial region, as well as difficulties in detecting fires located under thick clouds, and a reduction in fire detection  
531 sensitivity at the scan edge sensitivity, leading to an underestimation of total regional BB emissions (Wang et al., 2018). In  
532 this paper, The FINN2.5 dataset (BB emission fluxes and AOPs) is consistently higher than the other datasets, with FINN2.5  
533 MOSVIS being the highest overall. FINN2.5 includes improved burned area calculations, uses year-specific land cover and  
534 vegetation datasets, updates fuel loads and EF, and can use multiple fire detection satellite inputs (e.g., MODIS and VIIRS),  
535 which may account for the improved BB emission fluxes. In the PSEA region, during wildfire events, the BB emissions from  
536 FINNv2.5 are consistently higher than the emissions provided by FINNv1.5, approximately twice as much as the latter, even  
537 when considering only MODIS fire detections. The increase in emissions is primarily attributed to the new treatment of burned  
538 areas (Wiedinmyer et al., 2023). Despite updates to input data, parameters, and processing methods, the FINN2.5 scheme tends  
539 to overestimate AOPs compared to observations. This overestimation may arise from inaccurate ecosystem identification (e.g.,  
540 tropical forests instead of shrublands or areas with fewer trees) and fuel load allocation (Pan et al., 2020). Furthermore, in  
541 tropical regions, the FINN scheme employs smoothing of fire detections to mitigate the impact of clouds, which could lead to

542 an overestimate of BB emissions (Wiedinmyer et al., 2011; 2023). QFED provides relatively higher OC concentrations, but  
543 lower total BB emissions, and the primary driving factors behind these differences are the assumed fuel types and related EF.  
544 Therefore, it is inappropriate to consider OC as the sole criterion for evaluating BB emission fluxes when comparing multiple  
545 BB emission inventories. Although the aerosol concentrations provided by QFED are larger than those of IS4FIRES and FEER,  
546 the simulated AOPs and DRF of this scheme are lower than those of the latter, which may be due to the influence of secondary  
547 pollutant emission precursors (NO<sub>2</sub>, NH<sub>3</sub>, etc.). Previous studies have often used an expansion of aerosols (BC+OC) in the BB  
548 emission inventories by a factor of 3-6 to assess the AOPs (Reddington et al., 2016; Marlier et al., 2013), and the simulation  
549 results from the QFED scheme above reveal that there may be significant uncertainties in this expanded aerosol (BC+OC)  
550 approach. Although GFED4.1s improves the detection of small fires, the agricultural EF = 2.3 g /kg<sup>-1</sup> is lower than in other  
551 emission inventories, which could result in an underestimation of AOPs simulated by WRF-Chem with the GFED scheme.  
552 Yin (2020) found that BB in the PSEA region from 2001 to 2018 was predominantly driven by agro-residue burning and  
553 shrubland fires while GFED4.1s underestimation of DM for both fires and the mismatch in vegetation types may have  
554 contributed to the underestimation of BB emission fluxes (Reddington et al., 2016). In general, FRP-based estimation methods,  
555 such as GFAS, FEER, QFED, and IS4FIRES, allow for a more direct estimation of fuel consumption from fire-release energy  
556 without the uncertainty associated with the estimation. However, in the PSEA region, when the FRP from MODIS inversion  
557 is observed at a nominal spatial resolution of 1 km at its nadir, it risks missing a large number of smaller fires, as well as  
558 missing fires that are obscured by clouds (Dong and Fu, 2015b), which may lead to an underestimation of the simulated AOPs.  
559 Furthermore, the representation of aerosols in the BB emission inventories is insufficient, including chemical components,  
560 size distribution of aerosols, aging processes, hygroscopic growth, vertical and horizontal transport (including the injection  
561 height of fire emissions), and oxidation state (Reddington et al., 2016) which can all lead to modeling biases in AOPs.  
562 Importantly, these attributes also have an impact on aerosols in cloud and radiative forcing.

带格式的: 上标

#### 563 4.2 Modeling Uncertainty and Calculation Bias

564 There may be uncertainties in the gas-phase chemistry and aerosol scheme selected to characterize BB aerosols in the model  
565 (e.g., growth of aerosol hygroscopicity, scale distributions, aging processes, wet and dry deposition, etc.), which may lead to  
566 inaccurate simulation results~~The representation of BB aerosols in the model is inadequate, including insufficient~~  
567 ~~characterization of aerosol size distribution, chemical composition, aging processes, vertical and horizontal transport~~  
568 ~~(including injection heights of fire emissions), and model errors in dry/wet deposition from the atmosphere (Palacios-Peña et~~  
569 ~~al., 2018; Reddington et al., 2016). Sensitivity experiments using the global aerosol model reveal that calculations of~~  
570 ~~hygroscopicity growth are most sensitive in simulating AOD (Reddington et al., 2016). The contribution of SOA formed~~  
571 ~~through the oxidation of VOCs in BB plumes is also a significant source of uncertainty (Jathar et al., 2014). In this study, we~~  
572 ~~employed the meteorological chemistry and aerosol scheme: MOZART-MOSAIC\_4bin\_aqueous, which includes aqueous-~~  
573 ~~phase chemistry and SOA, but this mechanism may lead to overestimation/underestimation of AOPs in the model. The smoke~~  
574 ~~plume rise model developed by Freitas et al. (2010) was used to vertically represent smoke plumes. Although all schemes~~

575 capture the vertical profiles of BB aerosol extinction from 0.5 km to 4 km altitude, some deviations still exist. Previous research  
576 has indicated that assuming all fire emissions injected at the top of the plume could be a worse assumption than prescribing  
577 surface-based emissions, which may lead to deviations in simulated AOPs (Mallia et al., 2018). The AEC is not characterized  
578 in all BB scenario simulations for 4-8 km, which may also lead to an underestimation of AOD or AAOD, and this high-level  
579 perturbation of AEC may come from the influence of external dust aerosols, so the model emission inventory should consider  
580 the effect of dust emissions. ~~Despite the influence of sea salt aerosols in the near-surface region of PSEA (Figure S4), the~~  
581 ~~contribution of sea salt aerosol to AOD is notably small, approximately 2% (Zeng et al., 2023). Additionally, Dong and Fu~~  
582 ~~(2015a) observed that the model, during the period from 2006 to 2010, accurately simulated BB AOD without incorporating~~  
583 ~~sea-salt emissions over the PSEA region. Consequently, our model does not consider sea-salt emission inventories. Others~~  
584 studies have also found that uncertainties in anthropogenic emission inventories can also lead to simulation errors in AOPs  
585 and DRF during wildfires in the PSEA region (Dong and Fu, 2015a). Although we used the latest version of EDGAR 2015  
586 data, there may be some underestimation of such emission inventories with a large number of incoming factories in the PSEA  
587 region (Yang, 2016). Additionally, ~~the inclusion of ARI and aerosol-cloud interactions (ACI) the inclusion of direct and~~  
588 ~~indirect radiation feedback~~ in the WRF-Chem model has been found to effectively improve the simulation of AOPs in  
589 European wildfire simulations (Palacios-Peña et al., 2019), whereas this study only incorporates ~~ARI aerosol direct radiative~~  
590 ~~feedback. ACI is concerned with aerosols altering the albedo and lifetime of clouds (Baró et al., 2016). Failure to account for~~  
591 ~~ACI may result in models that do not accurately simulate cloud droplet numbers and sizes, lifetimes, and radiative balances,~~  
592 ~~with implications for climate and atmospheric AOPs (Gao et al., 2022) In the calculation of the AOPs, uncertainties associated~~  
593 ~~with the optical properties of the assumed BB aerosols, such as their refractive index, may also lead to biases in the AOPs.~~  
594 There is some uncertainty in the AOD from the VIIRS satellite inversion and in the SSA and AAOD from the TROPOMI  
595 inversion due to cloud cover effects in the PSEA region, which may also lead to biased assessments. In addition, the closest  
596 proximity method used in the gridding process of BB emission inventories can also lead to some calculation errors.

## 597 5. Summary and Conclusion

598 This study conducted sensitivity analyses to simulate AOPs and DRF in the PSEA region using eight commonly global BB  
599 emission inventories (GFED, FINN1.5, FINN2.5 MOS, FINN2.5 MOSVIS, GFAS, FEER, QFED, IS4FIRES) and the WRF-  
600 Chem model. The main findings can be summarized below.

601 Regarding BB emissions in the PSEA region, high OC emissions in all datasets (BB) are mainly concentrated in the northern  
602 parts of Laos, Cambodia, and Thailand, and in eastern Myanmar, with a difference in emissions of about a factor of 9 (0.295-  
603 2.533  $\text{Tg M}^{-1}\text{Tg/M}$ ), an overall mean and standard deviation of  $1.09 \pm 0.83 \text{ Tg M}^{-1}\text{Tg/M}$  and a CV of 76%, respectively. Those  
604 high BB emissions are primarily from savanna and agricultural fires. OC emissions in GFED and GFAS are significantly lower  
605 than in the other inventories. This is attributed to lower DM and agricultural fire EF in GFED, while DM is underestimated in  
606 GFAS. The OC in FINN2.5 VISMOS is about twice as high as those in FINN1.5, which is explained by the difference in DM

607 rather than EF. Total aerosol emissions are relatively high in the FINN scenarios (v1.5 and 2.5) compared to the other scenarios.  
608 Although the "top-down" emission inventories (GFAS, FEER, QFED, IS4FIRES) are constrained by the AOD from MODIS,  
609 the total aerosol emission flux is still insufficient.

610 The AOD from VIIRS (DB algorithm) demonstrates the best ability to retrieve the AOD compared to AERONET data. An  
611 evaluation of the AOPs in the PSEA region during March 2019 reveals different performances between observations (VIIRS,  
612 TROPOMI, AERONET) and BB emission inventories. When comparing the AOD simulated by WRF-Chem with the observed  
613 AOD from VIIRS, the FINN1.5, FEER, QFED, and IS4FIRES schemes show a better ability to reproduce high aerosol  
614 concentrations in the HAOD region, the GFED and GFAS schemes show limitations in characterizing these regions. The FINN  
615 (v1.5 and 2.5) schemes tend to overestimate AOD in the region, while other schemes underestimate AOD. The comparison  
616 with AERONET data further highlights the performance of different BB emission scenarios, with the FINN1.5 and IS4FIRES  
617 scenarios generally showing better agreement with observations. For AAOD comparison, it was found that the WRF-Chem  
618 simulations with different BB scenarios were less capable of simulating AAOD than AOD. The unsatisfactory performance of  
619 the GFED, GFAS, and QFED schemes may be due to low concentrations of absorbing aerosols or inaccuracies in the spatial  
620 distribution of BB emissions. Among the evaluated BB scenarios, the FINN1.5 schemes generally performed better in  
621 representing AAOD. Particularly, the FINN2.5 MOSVIS scheme, due to the incorporation of improved local time and inclusion  
622 of small fires from VIIRS, exhibits the best R with the simulated AOD and AAOD relative to observations. CALIPSO  
623 observations versus AEC simulated by WRF-Chem suggest that the smoke plume rise model can reproduce the minimum and  
624 maximum smoke plume heights of wildfire aerosols. However, the FINN (v1.5 and 2.5) schemes tend to overestimate the AEC  
625 compared to CALIPSO, while the other scenarios underestimate it. Regarding the DRF, the spatial distribution of the SW  
626 radiative disturbances due to BB aerosols closely follows the pattern of the AOD. the FINN (v1.5 and 2.5) schemes exhibit a  
627 stronger cooling effect at TOA, which may be due to the higher BC concentration in its emissions. In the HAOD region, BB  
628 aerosols exhibited a daytime SW radiative forcing of  $-32.60 \pm 24.50 \text{ W m}^{-2} \text{ W/m}^2$  at the SFC, positive forcing ( $1.70 \pm 1.40 \text{ W m}^{-2} \text{ W/m}^2$ )  
629  $\text{W/m}^2$ ) in the ATM, and negative forcing ( $-30.89 \pm 23.6 \text{ W m}^{-2} \text{ W/m}^2$ ) at the TOA. Overall, the FINN scenarios (especially  
630 FINN2.5) result in an overestimation of the AOPs in the PSEA region due to an overestimation of DM rather than EF, which  
631 in turn may lead to an overestimation of the DRF. Although the FINN2.5 MOSVIS scenario presents an overestimation of  
632 AOPs, the R is the best. Although the "top-down" emission inventory (GFAS, FEER, QFED, IS4FIRES) is constrained by the  
633 AOD from MODIS, the total aerosol emission flux is still insufficient, which leads to an underestimation of the AOPs modeled  
634 by WRF-Chem in the PSEA region. In addition, uncertainties in anthropogenic emissions, dust emissions, and vertical  
635 distribution of aerosol concentrations, may be attributed to differences from simulations versus observations during the wildfire  
636 period in the PSEA region.

637 Additional evaluations of satellite-based fire emission inventories, particularly in large BB source regions (PSEA), would  
638 contribute to a deeper understanding of the uncertainties associated with fire emissions. In the PSEA region, greater attention  
639 should be given to the impacts of small fires, cloud cover, different ecosystem types, and EF during various burning stages  
640 and ecosystem types on the inversion of BB emission inventories. To further explore the subsequent effects of BB emissions

641 (e.g., AOPs and radiative forcing), additional investigation of fire aerosol aging and treatment uncertainties (e.g., injection  
642 height, mixing state, SOA formation) are needed. Our study demonstrates that the uncertainty in BB emission inventories is  
643 an important factor influencing the WRF-Chem simulation of air quality and climate during wildfires, although the limitations  
644 of the model itself should not be overlooked. In the future, we will conduct additional sensitivity experiments and utilize more  
645 observational data to further validate the aforementioned uncertainties.  
646

#### 647 **Data availability**

648 Global Fire Emissions Database, Version 4.1 (GFEDv4.1) are available at <https://doi.org/10.3334/ORNLDAAC/1293>  
649 (Randerson et al., 2017); The Fire INventory from NCAR (FINN, including version 1.5 and 2.5) data files can be downloaded  
650 from <https://www.aom.ucar.edu/Data/fire/> (Wiedinmyer et al., 2011); CAMS global biomass burning emissions based on fire  
651 radiative power (GFAS v1.2) at <https://ads.atmosphere.copernicus.eu/cdsapp#!/dataset/cams-global-fire-emissions-gfas>  
652 (Rémy et al., 2017); Fire Energetics and Emissions Research version 1.0 (FEER) data files can be downloaded from  
653 <https://feer.gsfc.nasa.gov/data/emissions/> (Ichoku and Ellison, 2014); Quick Fire Emissions Dataset version 2.5 release 1  
654 (QFED) data can be accessed from <https://portal.nccs.nasa.gov/datashare/iesa/aerosol/emissions/QFED/v2.5r1/> (Koster et al.,  
655 2015), and Integrated Monitoring and Modelling System for Wildland FIRES Project version 2.0 (IS4FIRES) data files can be  
656 downloaded from <http://silam.fmi.fi/thredds/catalog/i4f20emis-arch/catalog.html> (Soares et al., 2015).

#### 657 **Author contributions**

658 Conceptualization, methodology, and writing—original draft, Y.B.J.; Y.B.J. and Y.M.L. designed the research framework and  
659 collected the materials; Y.B.J. calculated the emissions and drew the figures; Y.M.L. and Y.B.J. analyzed the results and wrote  
660 the paper with inputs from all authors; All authors contributed to the discussion and improvement of the paper; Supervision,  
661 Q.F.

#### 662 **Financial support**

663 This work was supported by the Guangdong Major Project of Basic and Applied Basic Research (Grant No.  
664 2020B0301030004), the National Key Research and Development Program of China (Grant No. 2019YFC0214605), Science  
665 and Technology Program of Guangdong Province (Science and Technology Innovation Platform Category) (Grant No.  
666 2019B121201002), and the National Natural Science Foundation of China (Grant No. 42075181).

667 **Competing interests**

668 The authors declare that they have no conflict of interest.

669 **References**

- 670 Akagi, S. K., Yokelson, R. J., Wiedinmyer, C., Alvarado, M. J., Reid, J. S., Karl, T., Crouse, J. D., and Wennberg, P. O.:  
671 Emission factors for open and domestic biomass burning for use in atmospheric models, *Atmos. Chem. Phys.*, 11, 4039-4072,  
672 10.5194/acp-11-4039-2011, 2011.
- 673 Andela, N., Kaiser, J. W., Heil, A., van Leeuwen, T. T., van der Werf, G. R., Wooster, M. J., Remy, S., and Schultz, M. G.:  
674 Assessment the Global Fire Assimilation System (GFASv1), MACC, Monitoring Atmospheric Composition and Climate II,  
675 urn:nbn:nl:ui:31-d103f7d8-9295-449f-8afd-6ae36c492b66, 2013.
- 676 Andreae, M. O.: Emission of trace gases and aerosols from biomass burning – an updated assessment, *Atmos. Chem. Phys.*,  
677 19, 8523-8546, 10.5194/acp-19-8523-2019, 2019.
- 678 Andreae, M. O. and Merlet, P.: Emission of trace gases and aerosols from biomass burning, 15, 955-966,  
679 <https://doi.org/10.1029/2000GB001382>, 2001.
- 680 Ångström, A.: On the Atmospheric Transmission of Sun Radiation and on Dust in the Air, *Geografiska Annaler*, 11, 156-166,  
681 10.1080/20014422.1929.11880498, 1929.
- 682 Archer-Nicholls, S., Lowe, D., Darbyshire, E., Morgan, W. T., Bela, M. M., Pereira, G., Trembath, J., Kaiser, J. W., Longo,  
683 K. M., Freitas, S. R., Coe, H., and McFiggans, G.: Characterising Brazilian biomass burning emissions using WRF-Chem with  
684 MOSAIC sectional aerosol, *Geosci. Model Dev.*, 8, 549-577, 10.5194/gmd-8-549-2015, 2015.
- 685 Baro, R., Palacios-Pena, L., Baklanov, A., Balzarini, A., Brunner, D., Forkel, R., Hirtl, M., Honzak, L., Perez, J. L., Pirovano,  
686 G., San Jose, R., Schroeder, W., Werhahn, J., Wolke, R., Zabkar, R., and Jimenez-Guerrero, P.: Regional effects of atmospheric  
687 aerosols on temperature: an evaluation of an ensemble of online coupled models, *Atmospheric Chemistry and Physics*, 17,  
688 9677-9696, 10.5194/acp-17-9677-2017, 2017.
- 689 Baró, R., Lorente cc lazas, R., Montávez, J. P., and Letters, P. J. J. G. R.: Biomass burning aerosol impact on surface winds  
690 during the 2010 Russian heatwave, 44, 1088-1094, 2016.
- 691 Baró, R., Maurer, C., Brioude, J., Arnold, D., and Hirtl, M.: The Environmental Effects of the April 2020 Wildfires and the  
692 Cs-137 Re-Suspension in the Chernobyl Exclusion Zone: A Multi-Hazard Threat, 12, 467, 2021.
- 693 Buchholz, R., Emmons, L., Tilmes, S., and Team, T.: CESM2. 1/CAM-chem Instantaneous Output for Boundary Conditions.  
694 UCAR/NCAR—Atmospheric Chemistry Observations and Modeling Laboratory, <https://doi.org/10.5065/NMP7-EP60>, 2019.
- 695 Carter, T. S., Heald, C. L., Jimenez, J. L., Campuzano-Jost, P., Kondo, Y., Moteki, N., Schwarz, J. P., Wiedinmyer, C.,  
696 Darmenov, A. S., da Silva, A. M., and Kaiser, J. W.: How emissions uncertainty influences the distribution and radiative  
697 impacts of smoke from fires in North America, *Atmos. Chem. Phys.*, 20, 2073-2097, 10.5194/acp-20-2073-2020, 2020.
- 698 Chapman, E. G., Gustafson, W. I., Easter, R. C., Barnard, J. C., Ghan, S. J., Pekour, M. S., and Fast, J. D.: Coupling aerosol-  
699 cloud-radiative processes in the WRF-Chem model: Investigating the radiative impact of elevated point sources, *Atmospheric  
700 Chemistry and Physics*, 9, 945-964, 10.5194/acp-9-945-2009, 2009.
- 701 Chen, L., Zhu, J., Liao, H., Gao, Y., Qiu, Y., Zhang, M., Liu, Z., Li, N., and Wang, Y.: Assessing the formation and evolution  
702 mechanisms of severe haze pollution in the Beijing–Tianjin–Hebei region using process analysis, *Atmos. Chem. Phys.*, 19,  
703 10845-10864, 10.5194/acp-19-10845-2019, 2019.
- 704 Cochrane, M. A.: *Tropical fire ecology: climate change, land use, and ecosystem dynamics*, Springer2009.
- 705 Crippa, P., Sullivan, R., Thota, A., and Pryor, S. J. J. o. G. R. A.: Sensitivity of Simulated Aerosol Properties Over Eastern  
706 North America to WRF-Chem Parameterizations, 124, 3365-3383, 2019.
- 707 Dong, X. and Fu, J. S.: Understanding interannual variations of biomass burning from Peninsular Southeast Asia, part I: Model  
708 evaluation and analysis of systematic bias, *Atmospheric Environment*, 116, 293-307,  
709 <https://doi.org/10.1016/j.atmosenv.2015.06.026>, 2015a.
- 710 Dong, X. and Fu, J. S.: Understanding interannual variations of biomass burning from Peninsular Southeast Asia, part II:  
711 Variability and different influences in lower and higher atmosphere levels, *Atmospheric Environment*, 115, 9-18,  
712 <https://doi.org/10.1016/j.atmosenv.2015.05.052>, 2015b.

713 Dubovik, O. and King, M. D. J. J. o. G. R. A.: A flexible inversion algorithm for retrieval of aerosol optical properties from  
714 Sun and sky radiance measurements, 105, 20673-20696, 2000.

715 Duc, H. N., Bang, H. Q., Quan, N. H., and Quang, N. X.: Impact of biomass burnings in Southeast Asia on air quality and  
716 pollutant transport during the end of the 2019 dry season, *Environmental Monitoring and Assessment*, 193, 565,  
717 10.1007/s10661-021-09259-9, 2021.

718 Emmons, L. K., Walters, S., Hess, P. G., Lamarque, J. F., Pfister, G. G., Fillmore, D., Granier, C., Guenther, A., Kinnison, D.,  
719 Laepple, T., Orlando, J., Tie, X., Tyndall, G., Wiedinmyer, C., Baughcum, S. L., and Kloster, S.: Description and evaluation  
720 of the Model for Ozone and Related chemical Tracers, version 4 (MOZART-4), *Geosci. Model Dev.*, 3, 43-67, 10.5194/gmd-  
721 3-43-2010, 2010.

722 Emmons, L. K., Schwantes, R. H., Orlando, J. J., Tyndall, G., Kinnison, D., Lamarque, J.-F., Marsh, D., Mills, M. J., Tilmes,  
723 S., Bardeen, C., Buchholz, R. R., Conley, A., Gettelman, A., Garcia, R., Simpson, I., Blake, D. R., Meinardi, S., and Pétron,  
724 G.: The Chemistry Mechanism in the Community Earth System Model Version 2 (CESM2), 12, e2019MS001882,  
725 <https://doi.org/10.1029/2019MS001882>, 2020.

726 Fan, W., Li, J., Han, Z., Wu, J., Zhang, S., Zhang, C., and Li, J.: Impacts of biomass burning in Southeast Asia on aerosols  
727 over the low-latitude plateau in China: An analysis of a typical pollution event, 11, 10.3389/fenvs.2023.1101745, 2023.

728 Fast, J. D., Gustafson Jr., W. I., Easter, R. C., Zaveri, R. A., Barnard, J. C., Chapman, E. G., Grell, G. A., and Peckham, S. E.:  
729 Evolution of ozone, particulates, and aerosol direct radiative forcing in the vicinity of Houston using a fully coupled  
730 meteorology-chemistry-aerosol model, 111, 10.1029/2005jd006721, 2006.

731 Ferrada, G. A., Zhou, M., Wang, J., Lyapustin, A., Wang, Y., Freitas, S. R., and Carmichael, G. R.: Introducing the VIIRS-  
732 based Fire Emission Inventory version 0 (VFEIv0), *Geosci. Model Dev.*, 15, 8085-8109, 10.5194/gmd-15-8085-2022, 2022.

733 Filonchyk, M., Peterson, M. P., and Sun, D.: Deterioration of air quality associated with the 2020 US wildfires, *Science of The*  
734 *Total Environment*, 826, 154103, <https://doi.org/10.1016/j.scitotenv.2022.154103>, 2022.

735 Freitas, S. R., Longo, K. M., Trentmann, J., and Latham, D.: Technical Note: Sensitivity of 1-D smoke plume rise models to  
736 the inclusion of environmental wind drag, *Atmos. Chem. Phys.*, 10, 585-594, 10.5194/acp-10-585-2010, 2010.

737 Freitas, S. R., Longo, K. M., Chatfield, R., Latham, D., Silva Dias, M. A. F., Andreae, M. O., Prins, E., Santos, J. C., Gielow,  
738 R., and Carvalho Jr, J. A.: Including the sub-grid scale plume rise of vegetation fires in low resolution atmospheric transport  
739 models, *Atmos. Chem. Phys.*, 7, 3385-3398, 10.5194/acp-7-3385-2007, 2007.

740 Gao, C., Xiu, A., Zhang, X., Tong, Q., Zhao, H., Zhang, S., Yang, G., and Zhang, M.: Two-way coupled meteorology and air  
741 quality models in Asia: a systematic review and meta-analysis of impacts of aerosol feedbacks on meteorology and air quality,  
742 *Atmos. Chem. Phys.*, 22, 5265-5329, 10.5194/acp-22-5265-2022, 2022.

743 Ge, C., Wang, J., and Reid, J. S.: Mesoscale modeling of smoke transport over the Southeast Asian Maritime Continent:  
744 coupling of smoke direct radiative effect below and above the low-level clouds, *Atmospheric Chemistry and Physics*, 14, 159-  
745 174, 10.5194/acp-14-159-2014, 2014.

746 Grell, G., Freitas, S. R., Stuefer, M., and Fast, J.: Inclusion of biomass burning in WRF-Chem: impact of wildfires on weather  
747 forecasts, *Atmospheric Chemistry and Physics*, 11, 5289-5303, 10.5194/acp-11-5289-2011, 2011.

748 Grell, G. A. and Dévényi, D. J. G. R. L.: A generalized approach to parameterizing convection combining ensemble and data  
749 assimilation techniques, 29, 38-31-38-34, 2002.

750 Grell, G. A., Peckham, S. E., Schmitz, R., McKeen, S. A., Frost, G., Skamarock, W. C., and Eder, B.: Fully coupled "online"  
751 chemistry within the WRF model, *Atmospheric Environment*, 39, 6957-6975, 10.1016/j.atmosenv.2005.04.027, 2005.

752 Guenther, A. B., Jiang, X., Heald, C. L., Sakulyanontvittaya, T., Duhl, T., Emmons, L. K., and Wang, X.: The Model of  
753 Emissions of Gases and Aerosols from Nature version 2.1 (MEGAN2.1): an extended and updated framework for modeling  
754 biogenic emissions, *Geosci. Model Dev.*, 5, 1471-1492, 10.5194/gmd-5-1471-2012, 2012.

755 Heil A., B. I.: ESA CCI ECV Fire Disturbance: D5.1 Product Validation and Intercomparison Report, version 2.1, 2020.

756 Hersbach, H., Bell, B., Berrisford, P., Biavati, G., Horányi, A., Muñoz Sabater, J., Nicolas, J., Peubey, C., Radu, R., and  
757 Rozum, I. J. C. c. s. c. d. s.: ERA5 hourly data on single levels from 1979 to present, 10, 2018.

758 Hu, Z. Y., Zhao, C., Huang, J. P., Leung, L. R., Qian, Y., Yu, H. B., Huang, L., and Kalashnikova, O. V.: Trans-Pacific  
759 transport and evolution of aerosols: evaluation of quasi-global WRF-Chem simulation with multiple observations,  
760 *Geoscientific Model Development*, 9, 1725-1746, 10.5194/gmd-9-1725-2016, 2016.

761 Huneus, N., Chevallier, F., and Boucher, O.: Estimating aerosol emissions by assimilating observed aerosol optical depth in  
762 a global aerosol model, *Atmos. Chem. Phys.*, 12, 4585-4606, 10.5194/acp-12-4585-2012, 2012.

763 Iacono, M. J., Delamere, J. S., Mlawer, E. J., Shephard, M. W., Clough, S. A., and Collins, W. D.: Radiative forcing by long-  
764 lived greenhouse gases: Calculations with the AER radiative transfer models, 113, <https://doi.org/10.1029/2008JD009944>,  
765 2008.

766 Ichoku, C. and Ellison, L.: Global top-down smoke-aerosol emissions estimation using satellite fire radiative power  
767 measurements, *Atmos. Chem. Phys.*, 14, 6643-6667, [10.5194/acp-14-6643-2014](https://doi.org/10.5194/acp-14-6643-2014), 2014.

768 Ichoku, C. and Kaufman, Y. J.: A method to derive smoke emission rates from MODIS fire radiative energy measurements,  
769 *IEEE Transactions on Geoscience and Remote Sensing*, 43, 2636-2649, [10.1109/TGRS.2005.857328](https://doi.org/10.1109/TGRS.2005.857328), 2005.

770 Janjić, Z. I.: The Step-Mountain Coordinate: Physical Package %J Monthly Weather Review, 118, 1429-1443,  
771 [https://doi.org/10.1175/1520-0493\(1990\)118<1429:TSMCPP>2.0.CO;2](https://doi.org/10.1175/1520-0493(1990)118<1429:TSMCPP>2.0.CO;2), 1990.

772 Jathar, S. H., Gordon, T. D., Hennigan, C. J., Pye, H. O. T., Pouliot, G., Adams, P. J., Donahue, N. M., and Robinson, A. L.:  
773 Unspeciated organic emissions from combustion sources and their influence on the secondary organic aerosol budget in the  
774 United States, 111, 10473-10478, [doi:10.1073/pnas.1323740111](https://doi.org/10.1073/pnas.1323740111), 2014.

775 Southeastern Asia Ignited by Agricultural Fires, last

776 Jin, Y., Ma, Y., Zhang, M., Liu, Y., Lu, X., Liu, B., Jin, S., Shen, A., Zhang, J., and Fan, Q.: Aerosol Characteristics during  
777 the COVID-19 Lockdown in China: Optical Properties, Vertical Distribution, and Potential Source, 14, 3336, 2022.

778 Jose, R. S., Pérez, J. L., González, R. M., Pecci, J., and Palacios, M.: Improving air quality modelling systems by using on-  
779 line wild land fire forecasting tools coupled into WRF/Chem simulations over Europe, *Urban Climate*, 22, 2-18,  
780 <https://doi.org/10.1016/j.uclim.2016.09.001>, 2017.

781 Kang, L., Chen, S., Huang, J., Zhao, S., Ma, X., Yuan, T., Zhang, X., and Xie, T.: The Spatial and Temporal Distributions of  
782 Absorbing Aerosols over East Asia, *Remote Sens.*, 9, 1050, 2017.

783 Koster, R. D., Darmenov, A. S., and da Silva, A. M.: The quick fire emissions dataset (QFED): Documentation of versions  
784 2.1, 2.2 and 2.4, 2015.

785 Kumar, R., Barth, M. C., Pfister, G. G., Naja, M., and Brasseur, G. P.: WRF-Chem simulations of a typical pre-monsoon dust  
786 storm in northern India: influences on aerosol optical properties and radiation budget, *Atmospheric Chemistry and Physics*,  
787 14, 2431-2446, [10.5194/acp-14-2431-2014](https://doi.org/10.5194/acp-14-2431-2014), 2014.

788 Lin, C.-Y., Zhao, C., Liu, X., Lin, N.-H., and Chen, W.-N.: Modelling of long-range transport of Southeast Asia biomass-  
789 burning aerosols to Taiwan and their radiative forcings over East Asia, *Tellus B: Chemical and Physical Meteorology*, 66,  
790 23733, [10.3402/tellusb.v66.23733](https://doi.org/10.3402/tellusb.v66.23733), 2014.

791 Liu, T., Mickley, L. J., Marlier, M. E., DeFries, R. S., Khan, M. F., Latif, M. T., and Karambelas, A.: Diagnosing spatial biases  
792 and uncertainties in global fire emissions inventories: Indonesia as regional case study, *Remote Sensing of Environment*, 237,  
793 111557, <https://doi.org/10.1016/j.rse.2019.111557>, 2020.

794 Ma, Y., Jin, Y., Zhang, M., Gong, W., Hong, J., Jin, S., Shi, Y., Zhang, Y., and Liu, B.: Aerosol optical properties of haze  
795 episodes in eastern China based on remote-sensing observations and WRF-Chem simulations, *Science of The Total  
796 Environment*, 757, 143784, [10.1016/j.scitotenv.2020.143784](https://doi.org/10.1016/j.scitotenv.2020.143784), 2021.

797 Mallet, M., Solmon, F., Nabat, P., Elguindi, N., Waquet, F., Bouniol, D., Sayer, A. M., Meyer, K., Roehrig, R., Michou, M.,  
798 Zuidema, P., Flamant, C., Redemann, J., and Formenti, P.: Direct and semi-direct radiative forcing of biomass-burning aerosols  
799 over the southeast Atlantic (SEA) and its sensitivity to absorbing properties: a regional climate modeling study, *Atmos. Chem.  
800 Phys.*, 20, 13191-13216, [10.5194/acp-20-13191-2020](https://doi.org/10.5194/acp-20-13191-2020), 2020.

801 Mallia, D. V., Kochanski, A. K., Urbanski, S. P., and Lin, J. C.: Optimizing Smoke and Plume Rise Modeling Approaches at  
802 Local Scales, 9, 166, 2018.

803 Marlier, M. E., DeFries, R. S., Voulgarakis, A., Kinney, P. L., Randerson, J. T., Shindell, D. T., Chen, Y., and Faluvegi, G.:  
804 El Niño and health risks from landscape fire emissions in southeast Asia, *Nature climate change*, 3, 131-136, 2013.

805 Martinez-Lozano, J., Utrillas, M., Tena, F., and Cachorro, V. J. S. E.: The parameterisation of the atmospheric aerosol optical  
806 depth using the Ångström power law, 63, 303-311, 1998.

807 EDGAR v5.0 emissions inventory speciated for the MOZART chemical mechanism, last

808 Mellor, G. L. and Yamada, T.: Development of a turbulence closure model for geophysical fluid problems, 20, 851-875,  
809 <https://doi.org/10.1029/RG020i004p00851>, 1982.

810 Monin, A. S. and Obukhov, A. M. J. C. G. I. A. S. U.: Basic laws of turbulent mixing in the surface layer of the atmosphere,  
811 151, e187, 1954.



812 Morrison, H., Curry, J. A., and Khvorostyanov, V. I.: A New Double-Moment Microphysics Parameterization for Application  
813 in Cloud and Climate Models. Part I: Description %J Journal of the Atmospheric Sciences, 62, 1665-1677,  
814 <https://doi.org/10.1175/JAS3446.1>, 2005.

815 Niu, G.-Y., Yang, Z.-L., Mitchell, K. E., Chen, F., Ek, M. B., Barlage, M., Kumar, A., Manning, K., Niyogi, D., Rosero, E.,  
816 Tewari, M., and Xia, Y.: The community Noah land surface model with multiparameterization options (Noah-MP): 1. Model  
817 description and evaluation with local-scale measurements, 116, <https://doi.org/10.1029/2010JD015139>, 2011.

818 Organization, W. M.: WMO El Niño/La Niña Update (May 2019), 2019.

819 Palacios-Peña, L., Baro, R., Luis Guerrero-Rascado, J., Alados-Arboledas, L., Brunner, D., and Jimenez-Guerrero, P.:  
820 Evaluating the representation of aerosol optical properties using an online coupled model over the Iberian Peninsula,  
821 Atmospheric Chemistry and Physics, 17, 277-296, [10.5194/acp-17-277-2017](https://doi.org/10.5194/acp-17-277-2017), 2017.

822 Palacios-Peña, L., Baró, R., Baklanov, A., Balzarini, A., Brunner, D., Forkel, R., Hirtl, M., Honzak, L., López-Romero, J. M.,  
823 Montávez, J. P. J. A. C., and Physics: An assessment of aerosol optical properties from remote-sensing observations and  
824 regional chemistry-climate coupled models over Europe, 18, 5021-5043, 2018.

825 Palacios-Peña, L., Jiménez-Guerrero, P., Baró, R., Balzarini, A., Bianconi, R., Curci, G., Landi, T. C., Pirovano, G., Prank,  
826 M., Riccio, A., Tuccella, P., and Galmarini, S.: Aerosol optical properties over Europe: an evaluation of the AQMEII Phase 3  
827 simulations against satellite observations, Atmos. Chem. Phys., 19, 2965-2990, [10.5194/acp-19-2965-2019](https://doi.org/10.5194/acp-19-2965-2019), 2019.

828 Pan, X., Ichoku, C., Chin, M., Bian, H., Darmenov, A., Colarco, P., Ellison, L., Kucsera, T., da Silva, A., Wang, J., Oda, T.,  
829 and Cui, G.: Six global biomass burning emission datasets: intercomparison and application in one global aerosol model,  
830 Atmos. Chem. Phys., 20, 969-994, [10.5194/acp-20-969-2020](https://doi.org/10.5194/acp-20-969-2020), 2020.

831 Randerson, J. T., Van Der Werf, G. R., Giglio, L., Collatz, G. J., and Kasibhatla, P. S.: Global Fire Emissions Database,  
832 Version 4.1 (GFEDv4), 10.3334/ORNLDAAC/1293, 2017.

833 Reddington, C. L., Conibear, L., Robinson, S., Knote, C., Arnold, S. R., and Spracklen, D. V.: Air Pollution From Forest and  
834 Vegetation Fires in Southeast Asia Disproportionately Impacts the Poor, 5, e2021GH000418,  
835 <https://doi.org/10.1029/2021GH000418>, 2021.

836 Reddington, C. L., Spracklen, D. V., Artaxo, P., Ridley, D. A., Rizzo, L. V., and Arana, A.: Analysis of particulate emissions  
837 from tropical biomass burning using a global aerosol model and long-term surface observations, Atmos. Chem. Phys., 16,  
838 11083-11106, [10.5194/acp-16-11083-2016](https://doi.org/10.5194/acp-16-11083-2016), 2016.

839 Reddington, C. L., Morgan, W. T., Darbyshire, E., Brito, J., Coe, H., Artaxo, P., Scott, C. E., Marsham, J., and Spracklen, D.  
840 V.: Biomass burning aerosol over the Amazon: analysis of aircraft, surface and satellite observations using a global aerosol  
841 model, Atmos. Chem. Phys., 19, 9125-9152, [10.5194/acp-19-9125-2019](https://doi.org/10.5194/acp-19-9125-2019), 2019.

842 Reid, J. S., Hyer, E. J., Johnson, R. S., Holben, B. N., Yokelson, R. J., Zhang, J., Campbell, J. R., Christopher, S. A., Di  
843 Girolamo, L., Giglio, L., Holz, R. E., Kearney, C., Miettinen, J., Reid, E. A., Turk, F. J., Wang, J., Xian, P., Zhao, G.,  
844 Balasubramanian, R., Chew, B. N., Janjai, S., Lagrosas, N., Lestari, P., Lin, N.-H., Mahmud, M., Nguyen, A. X., Norris, B.,  
845 Oanh, N. T. K., Oo, M., Salinas, S. V., Welton, E. J., and Liew, S. C.: Observing and understanding the Southeast Asian  
846 aerosol system by remote sensing: An initial review and analysis for the Seven Southeast Asian Studies (7SEAS) program,  
847 Atmospheric Research, 122, 403-468, <https://doi.org/10.1016/j.atmosres.2012.06.005>, 2013.

848 Rémy, S., Veira, A., Paugam, R., Sofiev, M., Kaiser, J. W., Marengo, F., Burton, S. P., Benedetti, A., Engelen, R. J., Ferrare,  
849 R., and Hair, J. W.: Two global data sets of daily fire emission injection heights since 2003, Atmos. Chem. Phys., 17, 2921-  
850 2942, [10.5194/acp-17-2921-2017](https://doi.org/10.5194/acp-17-2921-2017), 2017.

851 Saide, P. E., Mena-Carrasco, M., Tolvett, S., Hernandez, P., and Carmichael, G. R.: Air quality forecasting for winter-time  
852 PM<sub>2.5</sub> episodes occurring in multiple cities in central and southern Chile, Journal of Geophysical Research-Atmospheres, 121,  
853 558-575, [10.1002/2015jd023949](https://doi.org/10.1002/2015jd023949), 2016.

854 Saide, P. E., Carmichael, G. R., Liu, Z., Schwartz, C. S., Lin, H. C., da Silva, A. M., and Hyer, E.: Aerosol optical depth  
855 assimilation for a size-resolved sectional model: impacts of observationally constrained, multi-wavelength and fine mode  
856 retrievals on regional scale analyses and forecasts, Atmospheric Chemistry and Physics, 13, 10425-10444, [10.5194/acp-13-  
857 10425-2013](https://doi.org/10.5194/acp-13-10425-2013), 2013.

858 Sayer, A. M., Hsu, N. C., Lee, J., Kim, W. V., and Dutcher, S. T.: Validation, Stability, and Consistency of MODIS Collection  
859 6.1 and VIIRS Version 1 Deep Blue Aerosol Data Over Land, 124, 4658-4688, <https://doi.org/10.1029/2018JD029598>, 2019.

860 Smirnov, A., Holben, B. N., Eck, T. F., Dubovik, O., and Slutsker, I.: Cloud-Screening and Quality Control Algorithms for  
861 the AERONET Database, *Remote Sensing of Environment*, 73, 337-349, [https://doi.org/10.1016/S0034-4257\(00\)00109-7](https://doi.org/10.1016/S0034-4257(00)00109-7),  
862 2000.

863 Soares, J., Sofiev, M., and Hakkarainen, J.: Uncertainties of wild-land fires emission in AQMEII phase 2 case study,  
864 *Atmospheric Environment*, 115, 361-370, <https://doi.org/10.1016/j.atmosenv.2015.01.068>, 2015.

865 Sofiev, M., Vankevich, R., Lotjonen, M., Prank, M., Petukhov, V., Ermakova, T., Koskinen, J., and Kukkonen, J.: An  
866 operational system for the assimilation of the satellite information on wild-land fires for the needs of air quality modelling and  
867 forecasting, *Atmos. Chem. Phys.*, 9, 6833-6847, [10.5194/acp-9-6833-2009](https://doi.org/10.5194/acp-9-6833-2009), 2009.

868 Su, X., Wei, Y., Wang, L., Zhang, M., Jiang, D., and Feng, L.: Accuracy, stability, and continuity of AVHRR, SeaWiFS,  
869 MODIS, and VIIRS deep blue long-term land aerosol retrieval in Asia, *Science of The Total Environment*, 832, 155048,  
870 <https://doi.org/10.1016/j.scitotenv.2022.155048>, 2022.

871 Torres, O., Jethva, H., Ahn, C., Jaross, G., and Loyola, D. G. J. A. M. T.: TROPOMI aerosol products: evaluation and  
872 observations of synoptic-scale carbonaceous aerosol plumes during 2018–2020, 13, 6789-6806, 2020.

873 Veeffkind, J. P., Aben, I., McMullan, K., Förster, H., de Vries, J., Otter, G., Claas, J., Eskes, H. J., de Haan, J. F., Kleipool, Q.,  
874 van Weele, M., Hasekamp, O., Hoogeveen, R., Landgraf, J., Snel, R., Tol, P., Ingmann, P., Voors, R., Kruizinga, B., Vink, R.,  
875 Visser, H., and Levelt, P. F.: TROPOMI on the ESA Sentinel-5 Precursor: A GMES mission for global observations of the  
876 atmospheric composition for climate, air quality and ozone layer applications, *Remote Sensing of Environment*, 120, 70-83,  
877 <https://doi.org/10.1016/j.rse.2011.09.027>, 2012.

878 Vongruang, P., Wongwises, P., and Pimonsree, S.: Assessment of fire emission inventories for simulating particulate matter  
879 in Upper Southeast Asia using WRF-CMAQ, *Atmospheric Pollution Research*, 8, 921-929,  
880 <https://doi.org/10.1016/j.apr.2017.03.004>, 2017.

881 Wang, J., Yue, Y., Wang, Y., Ichoku, C., Ellison, L., and Zeng, J.: Mitigating Satellite-Based Fire Sampling Limitations in  
882 Deriving Biomass Burning Emission Rates: Application to WRF-Chem Model Over the Northern sub-Saharan African Region,  
883 123, 507-528, <https://doi.org/10.1002/2017JD026840>, 2018.

884 Wiedinmyer, C., Akagi, S. K., Yokelson, R. J., Emmons, L. K., Al-Saadi, J. A., Orlando, J. J., and Soja, A. J.: The Fire  
885 INventory from NCAR (FINN): a high resolution global model to estimate the emissions from open burning, *Geosci. Model  
886 Dev.*, 4, 625-641, [10.5194/gmd-4-625-2011](https://doi.org/10.5194/gmd-4-625-2011), 2011.

887 Wiedinmyer, C., Kimura, Y., McDonald-Buller, E. C., Emmons, L. K., Buchholz, R. R., Tang, W., Seto, K., Joseph, M. B.,  
888 Barsanti, K. C., Carlton, A. G., and Yokelson, R.: The Fire Inventory from NCAR version 2.5: an updated global fire emissions  
889 model for climate and chemistry applications, *EGU sphere*, 2023, 1-45, [10.5194/egusphere-2023-124](https://doi.org/10.5194/egusphere-2023-124), 2023.

890 Wu, J., Bei, N., Hu, B., Liu, S., Zhou, M., Wang, Q., Li, X., Lang, L., Tian, F., Liu, Z. J. A. C., and Physics: Aerosol–radiation  
891 feedback deteriorates the wintertime haze in the North China Plain, 19, 8703-8719, 2019.

892 Yadav, I. C., Linthoingambi Devi, N., Li, J., Syed, J. H., Zhang, G., and Watanabe, H.: Biomass burning in Indo-China  
893 peninsula and its impacts on regional air quality and global climate change-a review, *Environmental Pollution*, 227, 414-427,  
894 <https://doi.org/10.1016/j.envpol.2017.04.085>, 2017.

895 Yang, C. J. B.: Relocating labour-intensive manufacturing firms from China to Southeast Asia: A preliminary investigation,  
896 3, 1-13, 2016.

897 Yevich, R. and Logan, J. A.: An assessment of biofuel use and burning of agricultural waste in the developing world, 17,  
898 <https://doi.org/10.1029/2002GB001952>, 2003.

899 Yin, S.: Biomass burning spatiotemporal variations over South and Southeast Asia, *Environment International*, 145, 106153,  
900 <https://doi.org/10.1016/j.envint.2020.106153>, 2020.

901 Zeng, X., Li, S., Xing, J., Yang, J., Wang, Q., Song, G., Teng, M., Zhou, D., and Lu, J.: CALIPSO-observed Southeast Asia  
902 biomass-burning influences on aerosol vertical structure in Guangdong-Hong Kong-Macao Greater Bay Area, *Atmospheric  
903 Research*, 289, 106755, <https://doi.org/10.1016/j.atmosres.2023.106755>, 2023.

904 Zhang, F., Wang, J., Ichoku, C., Hyer, E. J., Yang, Z., Ge, C., Su, S., Zhang, X., Kondragunta, S., Kaiser, J. W., Wiedinmyer,  
905 C., and da Silva, A.: Sensitivity of mesoscale modeling of smoke direct radiative effect to the emission inventory: a case study  
906 in northern sub-Saharan African region, *Environmental Research Letters*, 9, 075002, [10.1088/1748-9326/9/7/075002](https://doi.org/10.1088/1748-9326/9/7/075002), 2014.

907 Zhang, L., Zhao, T., Gong, S., Kong, S., Tang, L., Liu, D., Wang, Y., Jin, L., Shan, Y., Tan, C., Zhang, Y., and Guo, X.:  
908 Updated emission inventories of power plants in simulating air quality during haze periods over East China, *Atmos. Chem.  
909 Phys.*, 18, 2065-2079, [10.5194/acp-18-2065-2018](https://doi.org/10.5194/acp-18-2065-2018), 2018.

910 Zhao, C., Liu, X., Ruby Leung, L., and Hagos, S.: Radiative impact of mineral dust on monsoon precipitation variability over  
 911 West Africa, *Atmos. Chem. Phys.*, 11, 1879-1893, 10.5194/acp-11-1879-2011, 2011.  
 912 Zhao, C., Leung, L. R., Easter, R., Hand, J., and Avise, J.: Characterization of speciated aerosol direct radiative forcing over  
 913 California, *Journal of Geophysical Research-Atmospheres*, 118, 2372-2388, 10.1029/2012jd018364, 2013.  
 914 Zhao, C., Liu, X., Leung, L. R., Johnson, B., McFarlane, S. A., Gustafson, W. I., Fast, J. D., and Easter, R.: The spatial  
 915 distribution of mineral dust and its shortwave radiative forcing over North Africa: modeling sensitivities to dust emissions and  
 916 aerosol size treatments, *Atmospheric Chemistry and Physics*, 10, 8821-8838, 10.5194/acp-10-8821-2010, 2010.  
 917 Zhu, J., Xia, X., Wang, J., Zhang, J., Wiedinmyer, C., Fisher, J. A., and Keller, C. A.: Impact of Southeast Asian smoke on  
 918 aerosol properties in Southwest China: First comparison of model simulations with satellite and ground observations, 122,  
 919 3904-3919, <https://doi.org/10.1002/2016JD025793>, 2017.  
 920

921 **Appendix A**

922 Abbreviations and Acronyms

AAOD	Absorbing aerosol optical depth
AEC	Aerosol extinction coefficient
AHAOD	Adjacent HAOD area
AOD	Aerosol optical depth
AOPs	Aerosol optical properties
ATM	In the atmosphere
BB	Biomass burning
BC	Black carbon
CALIPSO	Cloud-Aerosol Lidar and Infrared Pathfinder Satellite Observation
CAM-chem	Community Atmosphere Model with Chemistry
DA	Downwind area
DRF	Direct radiative forcing
DM	Dry matter
EDGAR	Emissions Database for Global Atmospheric Research
EF	Emission factors
FEER	Fire Energetics and Emissions Research
FINN	Fire INventory from NCAR
FRP	Fire radiative power
GEOS-Chem	Goddard Earth Observing System-Chemistry
GFAS	Global Fire Assimilation System
GFED	Global Fire Emissions Database
HAOD	High AOD

IS4FIRES	Integrated Monitoring and Modelling System for Wildland FIRES Project
LW	Longwave
MEGAN	Model of Emissions of Gases and Aerosols from Nature
MODIS	Moderate Resolution Imaging Spectroradiometer
MOSAIC	Model for Simulating Aerosol Interactions and Chemistry
MOZART	The Model for Ozone and Related chemical Tracers
NMHCs	Non-methane hydrocarbons
NMVOCs	Non-methane volatile organic compounds
OC	Organic carbon
OVOCs	Oxygenated volatile organic compounds
PSEA	Peninsular Southeast Asia
PM	Particulate matter
QFED	Quick Fire Emissions Dataset
RH2	2 m relative humidity
SFC	At the surface
SOA	Secondary organic aerosol
SSA	Single scattering albedo
SW	Shortwave
T2	2 m temperature
TOA	The top of the atmosphere
TPM	Total particle matter
VIIRS	Visible Infrared Imaging Radiometer Suite
WS10	10 m wind speed

923  
924

925 Tables

926 **Table 1. Comprehensive comparison of eight BB emission inventories globally in terms of different methodological details and**  
 927 **species, where Bottom-up approach to construct emission inventories are GFED v4.1s, FINN v1.5, FINN v2.5 MOS, FINN v2.5**  
 928 **MOSVIS, and others are Top-down approach.**

BB dataset	Resolution Temporal	Data source	EF reference (s)Main- <del>EF</del> <sup>a</sup>	OVOCs <sup>b</sup>	NMHCs <sup>c</sup>	Gases	Aerosols
GFED v4.1s	0.25°x 0.25°	MODIS C5	Akagi et al. (2011), Andreae and Merlet (2001) with updates	CH <sub>3</sub> COCHO, CH <sub>3</sub> COOH,etc	C <sub>2</sub> H <sub>4</sub> ,C <sub>2</sub> H <sub>6</sub> , C <sub>3</sub> H <sub>8</sub> , etc	CO, NO <sub>x</sub> , SO <sub>2</sub> , NH <sub>3</sub>	OC, BC, PM <sub>2.5</sub>
	3-hourly						
	daily						
FINN v1.5	1 km <sup>2</sup>	MODIS C6	Akagi et al. (2011), Andreae and Merlet (2001)	CH <sub>3</sub> COCHO, CH <sub>3</sub> COOH,etc	C <sub>2</sub> H <sub>4</sub> ,C <sub>2</sub> H <sub>6</sub> , C <sub>3</sub> H <sub>8</sub> , etc	CO, NO <sub>x</sub> , SO <sub>2</sub> , NH <sub>3</sub>	OC, BC, PM <sub>2.5</sub> ,PM <sub>10</sub>
	Daily						
FINN v2.5 MOS	1 km <sup>2</sup>	MODIS C6	Akagi et al. (2011), Wiedinmyer et al (2011)	CH <sub>3</sub> COCHO, CH <sub>3</sub> COOH,etc	C <sub>2</sub> H <sub>4</sub> ,C <sub>2</sub> H <sub>6</sub> , C <sub>3</sub> H <sub>8</sub> , etc	CO, NO <sub>x</sub> , SO <sub>2</sub> , NH <sub>3</sub>	OC, BC, PM <sub>2.5</sub> , PM <sub>10</sub>
	Daily						
FINN v2.5 MOSVIS	1 km <sup>2</sup>	MODIS C6	Akagi et al. (2011), Wiedinmyer et al (2011)	CH <sub>3</sub> COCHO, CH <sub>3</sub> COOH,etc	C <sub>2</sub> H <sub>4</sub> ,C <sub>2</sub> H <sub>6</sub> , C <sub>3</sub> H <sub>8</sub> , etc	CO, NO <sub>x</sub> , SO <sub>2</sub> , NH <sub>3</sub>	OC, BC, PM <sub>2.5</sub> , PM <sub>10</sub>
	Daily						
GFAS v1.2	0.1°x 0.1°	MODIS C6	Akagi et al. (2011)	CH <sub>3</sub> COCHO, CH <sub>3</sub> COOH,etc	C <sub>2</sub> H <sub>4</sub> ,C <sub>2</sub> H <sub>6</sub> , C <sub>3</sub> H <sub>8</sub> , etc	CO, NO <sub>x</sub> , SO <sub>2</sub> , NH <sub>3</sub>	OC, BC, PM <sub>2.5</sub>
	Daily						
FEER v1.0-G1.2	0.1°x 0.1°	GFAS v1.2	Andreae and Merlet (2001)	CH <sub>3</sub> COCHO, CH <sub>3</sub> COOH,etc	C <sub>2</sub> H <sub>4</sub> ,C <sub>2</sub> H <sub>6</sub> , C <sub>3</sub> H <sub>8</sub> , etc	CO, NO <sub>x</sub> , SO <sub>2</sub> , NH <sub>3</sub>	OC, BC, PM <sub>2.5</sub>
	Daily						
QFED v2.5r1	0.1°x 0.1°	MODIS C6	Akagi et al., (2011), Andreae and Merlet, (2001)	CH <sub>3</sub> COCHO, CH <sub>3</sub> COOH,etc	C <sub>2</sub> H <sub>6</sub> ,C <sub>3</sub> H <sub>6</sub> , C <sub>3</sub> H <sub>8</sub> , etc	CO, NO <sub>x</sub> , SO <sub>2</sub> , NH <sub>3</sub>	OC, BC, PM <sub>2.5</sub>
	Daily						
IS4FIRES v2.0	0.1°x 0.1°	MODIS C6	Akagi et al. (2011), Sofiev et al., (2009)	NA	NA	NA	TPM <sup>d</sup>
	3-hourly						
	2000-Present						

929 <sup>a</sup>The main references for Emission factors (EF) used in the BB emission database.

930 <sup>b</sup>Oxygenated volatile organic compounds (OVOCs) contain C, H, and O. examples include alcohols, aldehydes, ketones, and organic  
 931 acids.

932 <sup>c</sup>Non-methane hydrocarbons (NMHCs) are defined as organic compounds excluding methane (CH<sub>4</sub>) that contain only C and H.

933 <sup>d</sup>The total particle matter (TPM) considers three different particle sizes (0.17 μm, 1.1 μm and 3 μm).

934 Notes: OVOCs and NMHCs together account for nearly all the gas-phase non-methane volatile organic compounds (NMVOC)  
 935 emitted by fires (Akagi et al., 2011). NA: Not available.

936 **Table 2. WRF-Chem AOD and AAOD vs. satellites evaluation in HAOD (97-110°E, 15-22.5°N) region during March 2019.**

BB Inventories	WRF-Chem vs. VIIRS			WRF-Chem vs. TROPOMI		
	MB	RMSE	R	MB	RMSE	R
GFED	-0.26	0.48	0.22	0.009	0.018	0.191
FINN1.5	0.39	0.71	0.27	0.056	0.071	0.190
FINN2.5 MOS	0.63	0.98	0.27	0.073	0.094	0.205
FINN2.5 MOSVIS	0.78	1.01	0.28	0.080	0.102	0.232
GFAS	-0.34	0.52	0.21	0.004	0.013	0.185
FEER	-0.12	0.44	0.25	0.020	0.029	0.213
QFED	-0.24	0.46	0.23	0.011	0.020	0.187
IS4FIRES	-0.14	0.43	0.27	0.018	0.028	0.208

937  
938  
939  
940  
941  
942  
943  
944  
945  
946  
947  
948  
949  
950  
951  
952  
953  
954  
955  
956  
957  
958

959  
960**Table 3. WRF-Chem AOD at 550 nm vs. AERONET in HAOD, AHAOD, and DA during the wildfire period, where HAOD includes Laos, Chiang Mai, Doi Ang Khang, Fang, Nong Khai, Son La, and Ubon Ratchathani stations.**

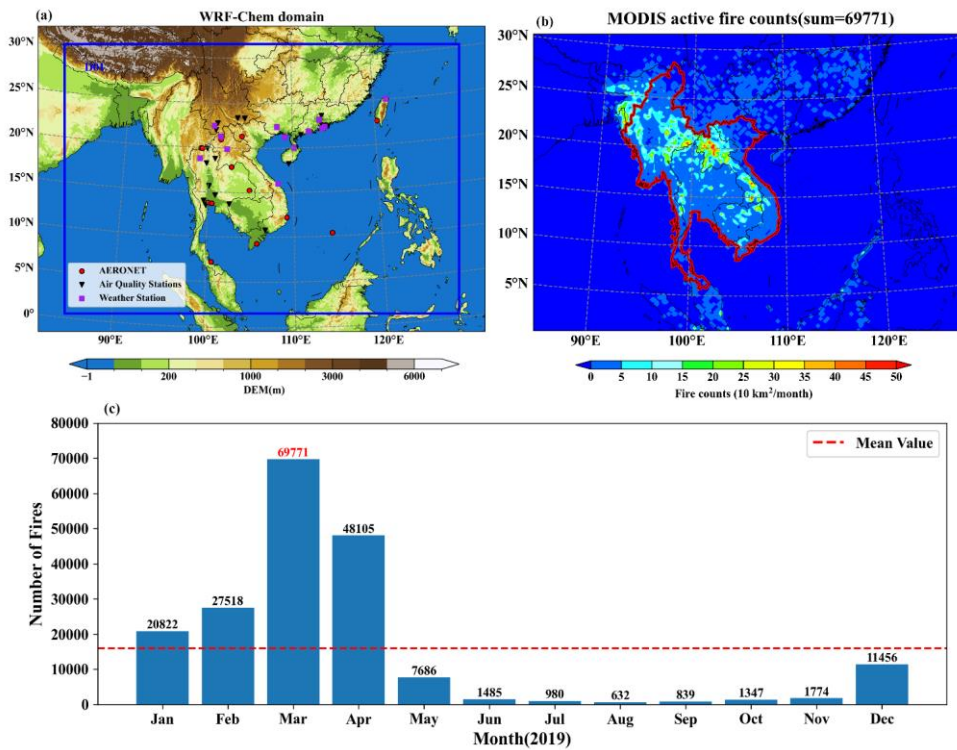
Stations	Variables	BB emission inventories							
		GFED	FINN1.5	FINN2.5 MOS	FINN2.5 MOSVIS	GFAS	FEER	QFED	IS4FIRES
Laos	R	0.74	0.9	0.9	0.81	0.7	0.84	0.79	0.85
	IOA	0.78	0.83	0.75	0.75	0.76	0.84	0.8	0.86
Chiang Mai	R	0.46	0.61	0.53	0.77	0.48	0.54	0.45	0.55
	IOA	0.75	0.79	0.74	0.82	0.73	0.77	0.76	0.78
Doi Ang Khang	R	0.48	0.66	0.66	0.8	0.49	0.64	0.52	0.63
	IOA	0.78	0.75	0.68	0.69	0.77	0.81	0.79	0.81
Fang	R	0.42	0.71	0.7	0.85	0.42	0.68	0.5	0.63
	IOA	0.71	0.81	0.77	0.82	0.7	0.73	0.71	0.75
Nong Khai	R	0.25	0.39	0.59	0.51	0.28	0.27	0.31	0.37
	IOA	0.73	0.71	0.69	0.65	0.71	0.72	0.73	0.74
Son La	R	0.5	0.75	0.76	0.64	0.43	0.81	0.64	0.64
	IOA	0.72	0.72	0.65	0.65	0.71	0.84	0.75	0.79
Ubon Ratchath ani	R	0.23	0.6	0.54	0.3	0.41	0.35	0.36	0.37
	IOA	0.68	0.64	0.61	0.58	0.64	0.69	0.66	0.69
AHBA	$\bar{R}$	0.44	0.51	0.48	0.24	0.53	0.52	0.55	0.52
	$\overline{IOA}$	0.73	0.69	0.66	0.63	0.72	0.76	0.75	0.74
DA	$\bar{R}$	0.43	0.41	0.39	0.48	0.44	0.44	0.46	0.39
	$\overline{IOA}$	0.69	0.71	0.69	0.71	0.69	0.71	0.70	0.70

Note: AHAOD and DA only contain the corresponding site mean R and IOA

961  
962

963  
964

### Figures



965

966

967

968

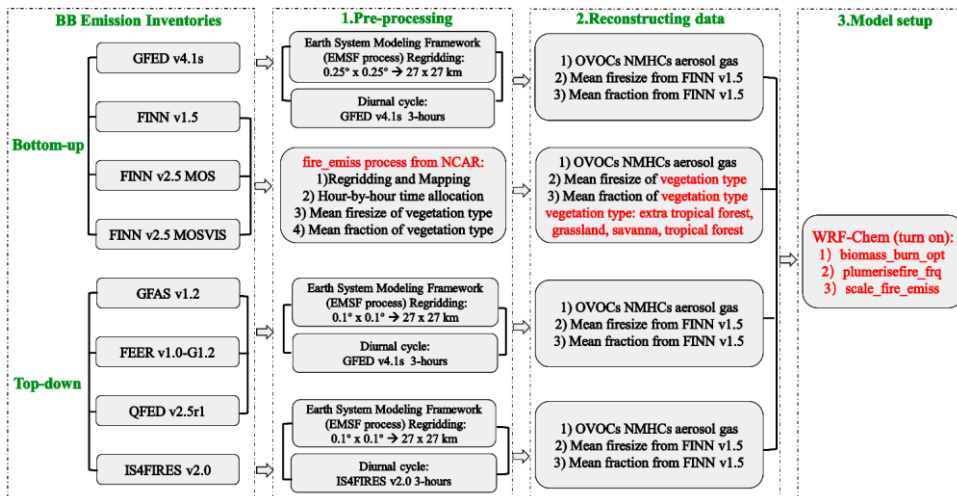
969

970

971

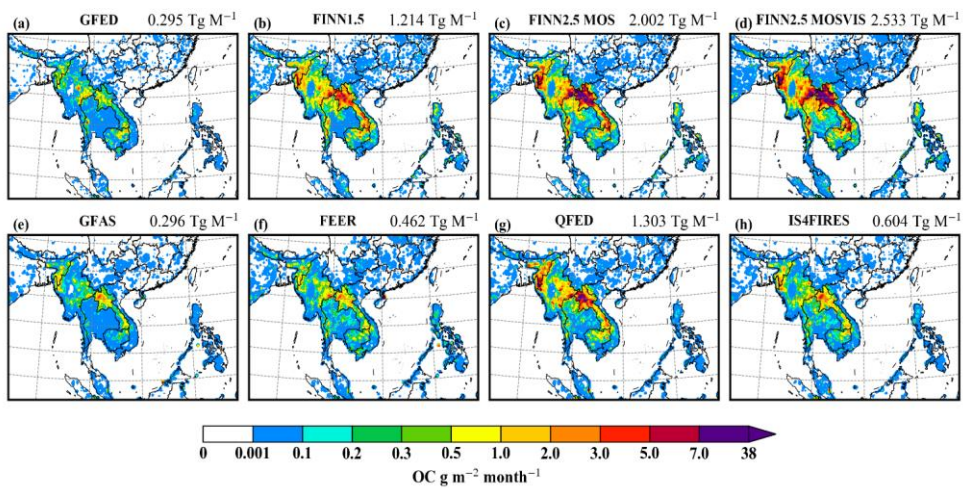
Figure 13. (a) WRF-Chem simulation domain (D01, blue line) and observation stations, which is mainly the PSEA region (purple line, including Vietnam, Thailand, Myanmar, Cambodia, and Laos), South China Sea, and South China region, where the red dots are AERONET stations, the black triangle crosses are air quality stations, and the purple rectangle blue crosses are meteorological stations. (b) Spatial distribution characteristics of fire points in PSEA (red line, including Vietnam, Thailand, Myanmar, Cambodia, and Laos) from MODIS satellite retrieval in March 2019. (c) Total fire counts in the PSEA region from Jan to Dec, 2019 (MODIS).





973  
974  
975  
976  
977  
978  
979  
980  
981  
982  
983  
984  
985

Figure 2. The flowchart illustrates the three processes of Pre-processing, Reconstructing data, and Model setup to put the eight BB emission inventories into the WRF-Chem simulation of AOPs and DRFs during the March 2019 wildfires in the PSEA region. The Pre-processing consisted of re-gridding and time allocation, where the FINNs scenario was processed using the fire\_emiss program from NCAR, while the grids generated by the other scenarios based on the FINN 1.5 scenario were spatially allocated using the EMSF program. The GFED, GFAS, FEER, and QFED have the same time allocations as GFED, and the remainder use self-contained time allocations. The Reconstructing data has three components: emissions (OVOCs, NMHCs, aerosol, and gas) composed by the MOZART-MOSAIC mechanism, fire size, and vegetation proportions (extratropical forest, grassland, savanna, tropical forest). Compared to the FINNs scheme, the missing compounds and aerosols from the other schemes were added based on the methodology of Jose et al. (2017), Andreae and Merlet (2001;2019). Eight BB emission inventories used the fire sizes provided by the FINN 1.5 scheme, as well as the vegetation proportions. The Model setup turned on BB simulations including the smoke plume rise.



986

987 Figure 3. The spatial distribution of eight BB emission inventories of OC in the study region, for (a-h): GFED, FINN1.5, FINN2.5  
 988 MOS, FINN2.5 MOSVIS, GFAS, FEER, QFED, IS4FIRES, and the total OC emissions in the PSEA region during March 2019.

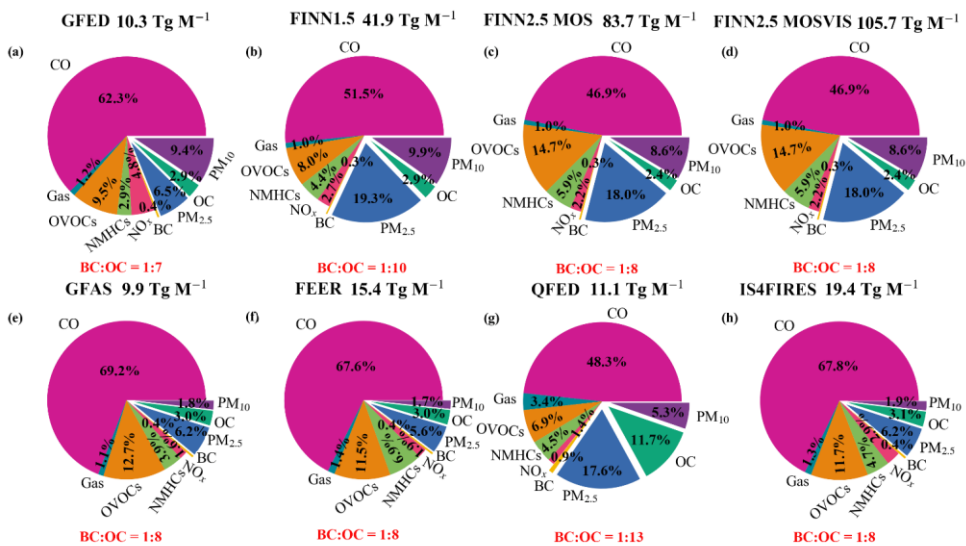


Figure 44. Total emissions and percentage composition of different substances in the eight BB emission inventories (after processing in Figure 2, i.e., the missing BB data has been supplemented.) over PSEA in the WRF-Chem model, which indicates the proportion of BC and OC, where "Gas" represents the combination of SO<sub>2</sub> and NH<sub>3</sub>. OVOCs contain C, H, and O compounds (ethanol (C<sub>2</sub>H<sub>5</sub>OH), formaldehyde (CH<sub>2</sub>O), acetaldehyde (CH<sub>3</sub>CHO), acetone (CH<sub>3</sub>COCH<sub>3</sub>), methanol (CH<sub>3</sub>OH), methyl ethyl ketone (MEK), pentanedial (C<sub>5</sub>H<sub>8</sub>O<sub>2</sub>), acetic acid (CH<sub>3</sub>COOH), cresol (C<sub>6</sub>H<sub>4</sub>(CH<sub>3</sub>)(OH)), glycerinaldehyde (GLYALD), methylglyoxal, methanal (MGLY), glyoxal (GLY)-(CH<sub>2</sub>COCHO), acetol (CH<sub>3</sub>COCH<sub>2</sub>OH), methacrolein, methyl vinyl ketone (MACR), methyl vinyl ketone (MVK)). NMHCs refer to organic compounds containing only C and H besides methane (CH<sub>4</sub>), including pentane (C<sub>5</sub>H<sub>12</sub>), butadiene (C<sub>4</sub>H<sub>6</sub>), ethylene (C<sub>2</sub>H<sub>4</sub>), ethane (C<sub>2</sub>H<sub>6</sub>), propane (C<sub>3</sub>H<sub>8</sub>), propylene (C<sub>3</sub>H<sub>6</sub>), toluene (C<sub>6</sub>H<sub>5</sub>(CH<sub>3</sub>)), lumped monoterpenes, as  $\alpha$ -pinene, decane (C<sub>10</sub>H<sub>16</sub>), isoprene (C<sub>5</sub>H<sub>8</sub>). NMHCs and OVOCs combined constitute nearly all of the non-methane volatile organic compounds (NMVOCs) emitted by wildfires. PM<sub>2.5</sub> is the PM<sub>2.5</sub> fraction excluding OC and BC. PM<sub>10</sub> is the PM<sub>10-2.5</sub> fraction.

带格式的: 字体:(默认)+西文正文(Times New Roman)

带格式的: 字体:(默认)+西文正文(Times New Roman)

带格式的: 字体:(默认)+西文正文(Times New Roman)

带格式的: 字体:(默认)+西文正文(Times New Roman), 下标

带格式的: 字体:(默认)+西文正文(Times New Roman)

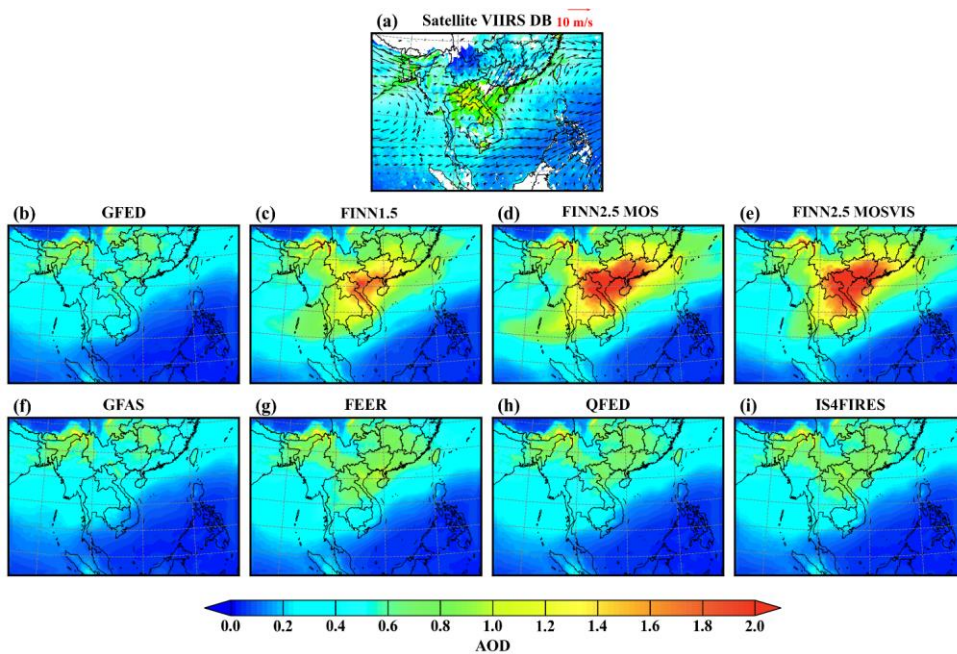
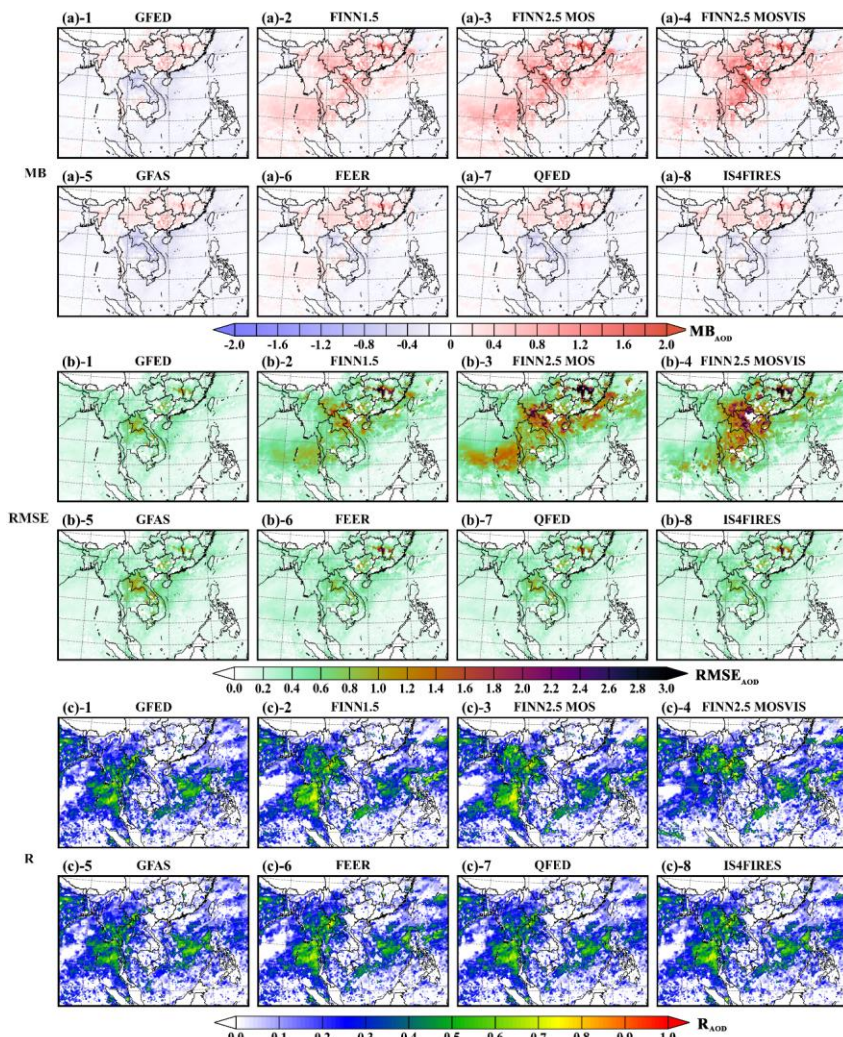


Figure 5. The daily mean AOD retrieved by the VIIRS satellite (a) transiting the PSEA region and the AOD simulated by WRF-Chem with eight corresponding BB emission inventories (b-i, GFED, FINN1.5, FINN2.5 MOS, FINN2.5 MOSVIS, GFAS, FEER, QFED, IS4FIRES) in the PSEA region during March 2019, where 950 hPa wind (vectors, m/s) based on March 2019 of ERA5 data.

1000  
 1001  
 1002  
 1003  
 1004  
 1005  
 1006  
 1007  
 1008  
 1009  
 1010  
 1011  
 1012  
 1013



1014

1015

1016

1017

1018

Figure 6. Spatial distribution of MB, RMSE, and R between AOD from VIIRS satellite vs. AOD simulated by WRF-Chem with 8 BB emission inventories (GFED, FINN1.5, FINN2.5 MOS, FINN2.5 MOSVIS, GFAS, FEER, QFED, IS4FIRES) in PSEA during March 2019, where (a)-1 to (a)-8 are the MB for the comparison of the eight BB scenarios, (b)-1 to (b)-8 are the RMSE for the comparison of the eight BB scenarios, (c)-1 to (c)-8 are the R for the comparison of the eight BB scenarios.

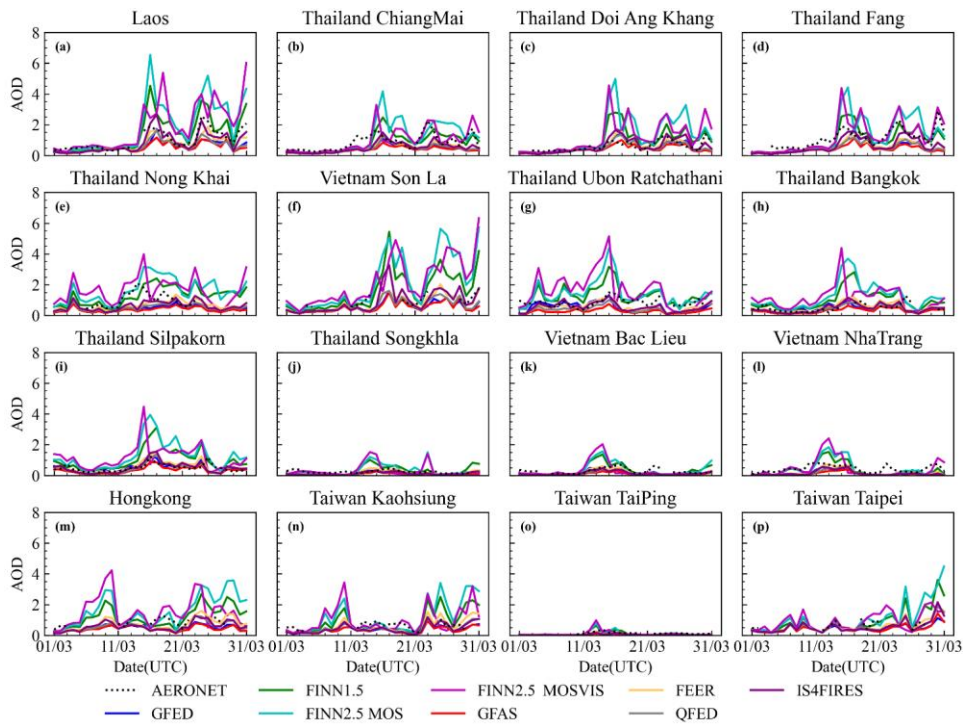


Figure 7. Time series of daily average AOD (550 nm) simulated by WRF-Chem including 8 BB emissions in March 2019 compared to 16 AERONET sites (a-p). These stations are divided into three categories, where the first category of stations is located within the HAOD range of satellite inversion (97-110°E, 15-22.5°N, a-g); The second type consists of observational sites located in adjacent high AOD regions (namely AHAOD, h-l); The third type encompasses observational sites situated within the downwind areas (namely DA, m-p). The legend line characterizes different BB simulation scenarios.

1033

Figure 8 consists of two Taylor diagrams, (a) and (b), comparing AERONET observations with WRF-Chem model results. Both diagrams plot Standard deviation (Normalized) on the x-axis and Correlation on the curved outer axis. A red dashed circle represents the 1:1 ratio. The legend identifies the following models and their symbols:

- GFED: Blue triangle
- FINN1.5: Green star
- FINN2.5 MOS: Cyan square
- FINN2.5 MOSVIS: Purple triangle
- GFAS: Red circle
- FEER: Yellow star
- QFED: Grey triangle
- IS4FIRES: Purple inverted triangle
- obs: Black circle

Diagram (a) shows AOD at 550 nm with a standard deviation axis from 0 to 2.25 and a correlation axis from 0.1 to 1.0. Diagram (b) shows AAOD at 500 nm with a standard deviation axis from 0 to 4.75 and a correlation axis from 0.1 to 1.0. The 'obs' point is at (1.0, 1.0) in both diagrams.

1034

1035 **Figure 8.** Taylor diagrams of (a) AERONET vs. WRF-Chem AOD at 550 nm and (b) AERONET vs. WRF-Chem AAOD at 500  
 1036 nm in the HAOD region (97-110°E, 15-22.5°N) during the wildfire period.

1037

39

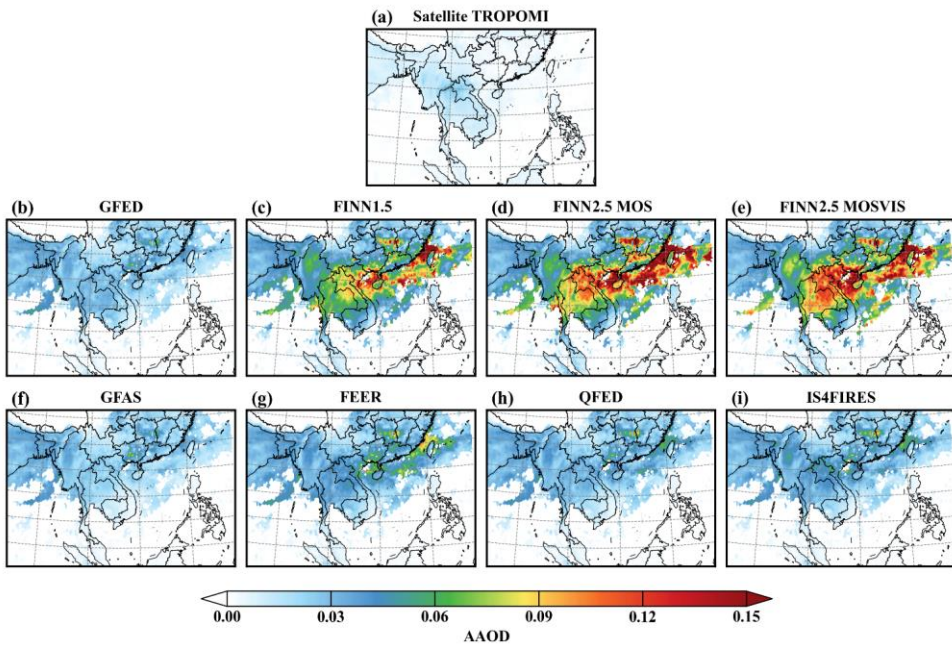


Figure 9. Spatial distribution of AAOD between Sentinel-5 TROPOMI satellite (a) vs. AAOD simulated by WRF-Chem with 8 BB emission inventories (b-i) during wildfire period in PSEA.

1038  
 1039  
 1040  
 1041  
 1042  
 1043  
 1044  
 1045  
 1046  
 1047  
 1048  
 1049  
 1050  
 1051  
 1052



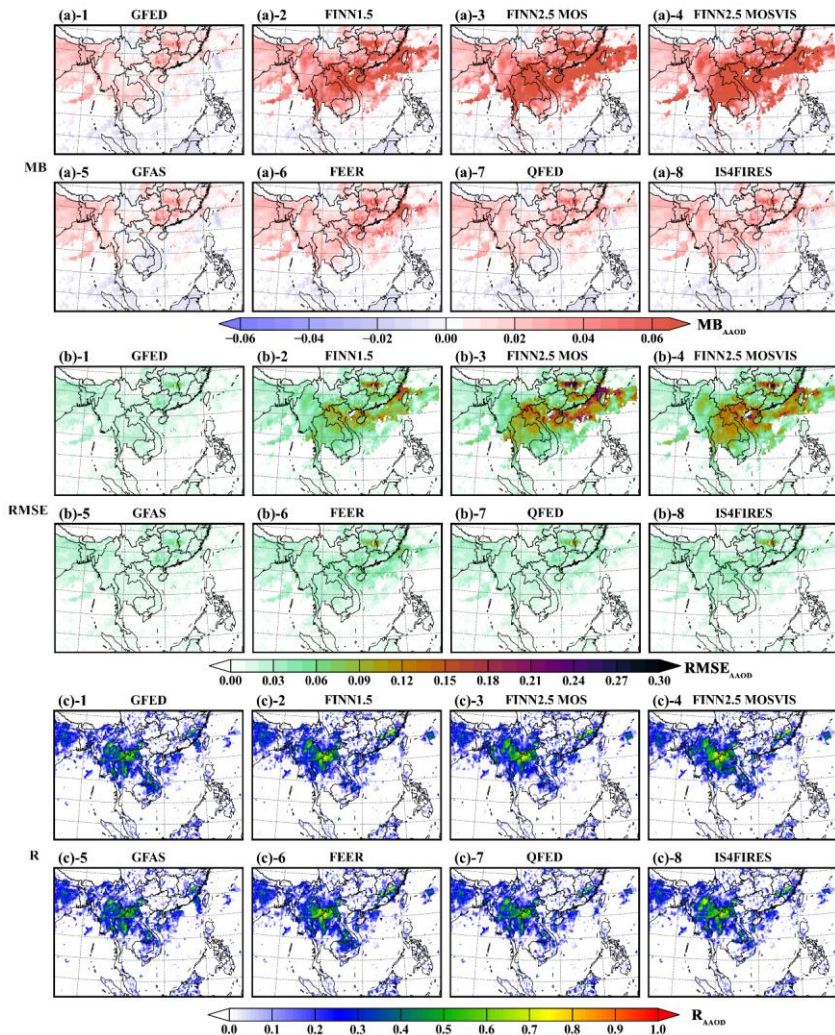
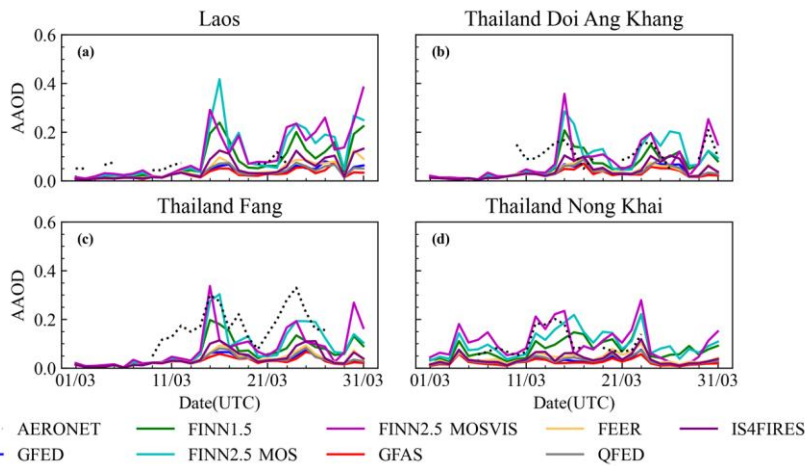
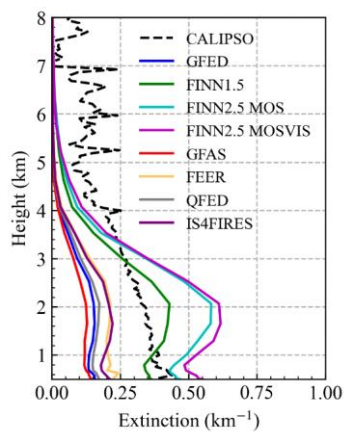


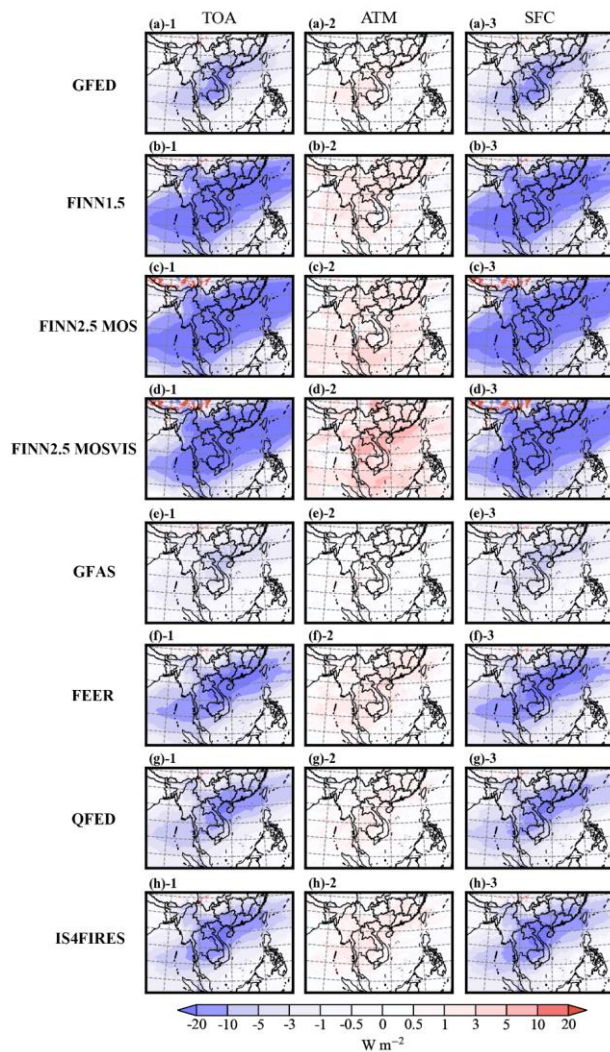
Figure 10. Spatial distribution of MB, RMSE, and R between AOD from VIIRS satellite vs. AOD simulated by WRF-Chem with 8 BB emission inventories (GFED, FINN1.5, FINN2.5 MOS, FINN2.5 MOSVIS, GFAS, FEER, QFED, IS4FIRES) in PSEA during March 2019, where (a)-1 to (a)-8 are the MB for the comparison of the eight BB scenarios, (b)-1 to (b)-8 are the RMSE for the comparison of the eight BB scenarios, (c)-1 to (c)-8 are the R for the comparison of the eight BB scenarios.



1058  
 1059 **Figure 11.** Comparisons of time series between daily mean AAOD at 500 nm measurements provided by four AERONET sites within  
 1060 the HAOD range and AAOD simulated by the nearest corresponding AERONET site using WRF-Chem adding different BB  
 1061 inventories, where the satellite inversions of both AOD > 1 and AAOD > 0.03 range 97-110°E, 15-22.5°N are called HAOD. The  
 1062 legend line is the same as in Figure 7.

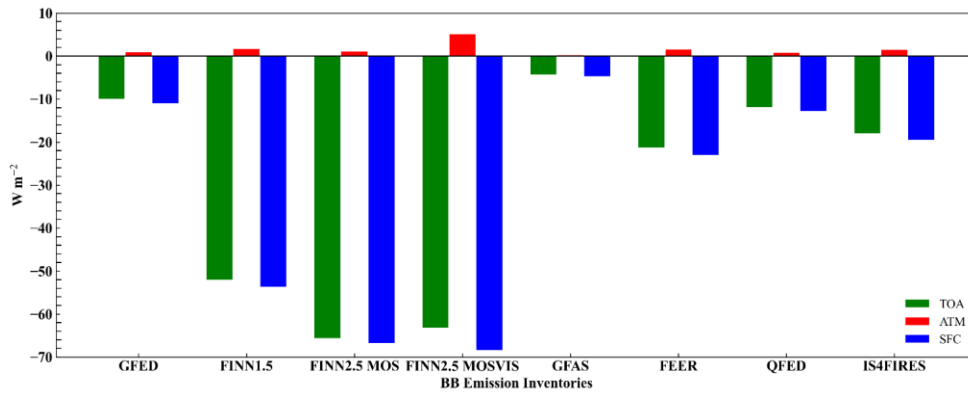


1063  
 1064 **Figure 12.** Vertical distributions of monthly mean aerosol extinction (550 nm) from WRF-Chem with different BB inventories and  
 1065 the corresponding CALIPSO retrieval (532nm) in HAOD (97-110°E, 15-22.5°N). The black dotted line indicates CALIPSO and the  
 1066 remaining lines are the same as in Figure 7.



1067  
1068  
1069  
1070

Figure 13. The average difference in clear-sky SW radiation fluxes (daytime) simulated with and without BB emission (GFED, FINN1.5, FINN2.5 MOS, FINN2.5 MOSVIS, GFAS, FEER, QFED, IS4FIRES) over the PSEA in March 2019 at the top of the atmosphere (TOA), ground surface (SFC), and in the atmosphere (ATM), Where (a)-(h) represent 8 emission inventories.



1071

1072

1073

1074

Figure 14. The average difference in clear-sky SW radiation fluxes (daytime) simulated with and without BB emission in the HAOD (97-110°E,15-22.5°N) region during March 2019.